THE ASTROPHYSICAL JOURNAL, 521:460–477, 1999 August 10

THE RISE OF KINK-UNSTABLE MAGNETIC FLUX TUBES AND THE ORIGIN OF δ-CONFIGURATION SUNSPOTS

Y. FAN
HAO, National Center for Atmospheric Research[1], P.O. Box 3000, Boulder, CO 80307
E. G. ZWEIBEL
JILA, University of Colorado at Boulder, Campus Box 440, Boulder, CO 80309-0440
M. G. LINTON AND G. H. FISHER
Space Sciences Laboratory, University of California at Berkeley, Berkeley, CA 94720
Received 1998 October 28; accepted 1999 March 23

ABSTRACT

We perform three-dimensional simulations of the rise of twisted magnetic flux tubes in an adiabatically stratified model solar convection zone. The initial flux tube in our simulations is a uniformly twisted, buoyant, horizontal tube located near the bottom of the stratified layer. The twist of the initial flux tube is described by a parameter α, which is defined as the angular rate of field-line rotation about the tube axis per unit length of the tube. We study the nonlinear evolution of the helical kink instability of the flux tube as it rises through the stratified layer. We find from our simulations that in order for the tube to develop significant kinking during its rise, the initial twist of the tube needs to be close to or greater than the critical limit (α_c) for the onset of the kink instability. If the initial twist is significantly below the critical limit (α below about 50% of α_c), we find essentially no kink development and the evolution is similar to the results from previous two-dimensional simulations of the rise of twisted, horizontal flux tubes. On the other hand, if the initial twist is sufficiently greater than the critical limit such that the *e*-folding period of the fastest growing kink mode is small compared to the rise time of the tube, we find sharp bending and distortion of the tube as a result of the nonlinear evolution of the kink instability. In this case, we find that due to the effect of gravitational stratification, the kinked flux tube arches upward and evolves into a buckled loop with a local change of tube orientation at the loop apex that exceeds 90° from the original direction of the tube. The emergence of this buckled loop can give rise to a compact magnetic bipole with polarity order inverted from the Hale polarity law, similar to the configuration often seen in δ spots. Furthermore, our simulations show that the writhing of the tube axis as a result of the kink instability stretches the flux tube and increases its buoyancy. Hence, the development of the kink instability can speed up the overall rise of the flux tube.

Subject headings: MHD — Sun: magnetic fields — sunspots

1. INTRODUCTION

Solar active regions are believed to be formed through the emergence of magnetic flux tubes from the base of the solar convection zone, where strong toroidal magnetic field is being generated by the dynamo mechanism. The qualitative picture is that an Ω-shaped loop of magnetic flux develops from the toroidal magnetic field and rises through the convection zone until its apex intersects the photosphere to form a bipolar magnetic region. Most of the bipolar magnetic regions on the solar surface are found to obey Hale's polarity rule (see, e.g., Zirin 1988, p. 307). This can be understood if the rising Ω loops roughly preserve the original orientation of the toroidal magnetic field at the base of the convection zone. It has recently become a popular notion, given the support from both observations (Lites et al. 1995; Leka et al. 1996; Lites & Low 1997) and theoretical arguments (McClymont & Fisher 1989; Low 1996; Moreno-Insertis & Emonet 1996; Fan, Zweibel, & Lantz 1998a; Matsumoto et al. 1998), that some flux tubes emerge from the solar interior already twisted and that the free magnetic energy released in large solar flares does not come from the energy built up through photospheric shearing motion but is rather already present in the emerging flux tubes. If the Ω-loop flux tube is sufficiently twisted, then it is subject to the current driven kink instability. Tanaka (1991) invoked a model of the emergence of a kinked (or knotted) magnetic flux tube to explain the observed evolution of the flare-active δ configuration sunspots. The so-called δ configuration describes a type of unusual active region in which sunspot umbrae of opposite polarities are pressed together in a common penumbra, and the polarity order is often inverted from Hale's polarity law. It is of interest to study how δ spots are formed, because they are known to be the most flare-productive active regions. The δ configuration suggests an abnormal emerging flux tube structure as compared to a simple Ω loop. The emergence of a kinked Ω loop is an appealing possibility because it can explain the inverted polarity order and the compactness of the structure.

Recently, Linton et al. (1996, 1998, 1999) and Fan et al. (1998b) have carried out theoretical investigations of kink-unstable flux tubes in a pressure-dominated (high β) plasma to study their possible role in the formation of δ-spot active regions. Linton et al. (1996) investigated the linear kink instability of uniformly twisted magnetic flux tubes confined by pressure in a high β plasma. Through three-dimensional MHD simulations, Linton et al. (1998, 1999) expand upon their linear calculations to study the nonlinear evolution of the kink unstable magnetic flux tubes. They investigated the kinked equilibrium configurations the flux tubes evolve into

[1] The National Center for Atmospheric Research is sponsored by the National Science Foundation.

as a result of the nonlinear growth of one or multiple unstable kink modes. Their simulations do not include the effect of gravity and stratification. In an effort to study the dynamic evolution of emerging magnetic flux tubes in the stratified solar convection zone, we have developed a three-dimensional anelastic MHD code. The anelastic formulation is suitable for studying slow, subsonic dynamic processes in the high-β plasma of the solar interior. In this paper, we use this three-dimensional anelastic MHD code to simulate the nonlinear evolution of the kink instability of a twisted magnetic flux tube as it rises buoyantly through a gravitationally stratified layer representing the solar convection zone. We do not attempt to model simultaneously the evolution of the Ω loop resulting from the undular Parker instability and the development of the kink instability on the Ω loop, because the wavelengths of the two instabilities are vastly different for flux tubes near the base of the convection zone. We model the rise of a relatively short segment of buoyant flux tube, which can be viewed as the apex portion of a rising Ω loop, and focus on studying the local kinked structure that can be formed as a result of the nonlinear evolution of the kink instability.

The remainder of the paper is organized as follows. Section 2 describes the basic anelastic numerical model used by our simulations. A more detailed description of the numerical algorithm used to solve the governing equations is given in the Appendix. Section 3 discusses the important physical timescales involved in the present problem. The results of the simulations are presented in § 4, and the conclusions are summarized in § 5.

2. THE NUMERICAL MODEL

The equations we solve with our numerical code are the anelastic form of the basic MHD equations:

$$\nabla \cdot (\rho_0 \boldsymbol{v}) = 0 , \tag{1}$$

$$\rho_0 \left[\frac{\partial \boldsymbol{v}}{\partial t} + (\boldsymbol{v} \cdot \nabla)\boldsymbol{v} \right] = -\nabla p_1 + \rho_1 \boldsymbol{g} + \frac{1}{4\pi} (\nabla \times \boldsymbol{B}) \times \boldsymbol{B} + \nabla \cdot \Pi , \tag{2}$$

$$\rho_0 T_0 \left[\frac{\partial s_1}{\partial t} + (\boldsymbol{v} \cdot \nabla)(s_0 + s_1) \right] = \nabla \cdot (K \rho_0 T_0 \nabla s_1) + \frac{1}{4\pi} \eta |\nabla \times \boldsymbol{B}|^2 + (\Pi \cdot \nabla) \cdot \boldsymbol{v} , \tag{3}$$

$$\nabla \cdot \boldsymbol{B} = 0 , \tag{4}$$

$$\frac{\partial \boldsymbol{B}}{\partial t} = \nabla \times (\boldsymbol{v} \times \boldsymbol{B}) - \nabla \times (\eta \nabla \times \boldsymbol{B}) , \tag{5}$$

$$\frac{\rho_1}{\rho_0} = \frac{p_1}{p_0} - \frac{T_1}{T_0} , \tag{6}$$

$$\frac{s_1}{c_p} = \frac{T_1}{T_0} - \frac{\gamma - 1}{\gamma} \frac{p_1}{p_0} . \tag{7}$$

The detailed derivation of the above equations can be found in many previous publications (e.g., Gilman & Glatzmaier 1981; Glatzmaier 1984; Lantz & Fan 1999). The anelastic formulation assumes a time-independent, background reference state of hydrostatic equilibrium and nearly adiabatic stratification described by $s_0(z)$, $p_0(z)$, $\rho_0(z)$, and $T_0(z)$, which are functions of height z only, and solves for the evolution of velocity $\boldsymbol{v}$, magnetic field $\boldsymbol{B}$, and the thermodynamic fluctuations s_1, p_1, ρ_1, and T_1, which represent perturbations from the reference state. In the above equations, Π is the viscous stress tensor given by

$$\Pi_{ij} \equiv \mu \left[\frac{\partial v_i}{\partial x_j} + \frac{\partial v_j}{\partial x_i} - \frac{2}{3} (\nabla \cdot \boldsymbol{v}) \delta_{ij} \right] , \tag{8}$$

and μ, K, and η denote, respectively, the dynamic viscosity, and thermal and magnetic diffusivities.

In these calculations, we use an adiabatically stratified polytrope as the reference state (so that the fluid is marginally stable to convection):

$$T_0(z) = T_r \left[1 - \frac{z}{(m+1)H_r} \right] , \tag{9}$$

$$\rho_0(z) = \rho_r \left[1 - \frac{z}{(m+1)H_r} \right]^m , \tag{10}$$

$$p_0(z) = p_r \left[1 - \frac{z}{(m+1)H_r} \right]^{m+1} , \tag{11}$$

where T_r, ρ_r, p_r, and H_r are, respectively, the values of T_0, ρ_0, p_0, and H_p (the pressure scale height) at $z = 0$, and m is the polytropic index which relates to the ratio of specific heats γ as $m = 1/(\gamma - 1)$. We assume an ideal gas with $\gamma = 5/3$ and $m = 1.5$.

We solve the three-dimensional anelastic MHD equations in a rectangular Cartesian domain with periodic boundary conditions in the horizontal directions and nonpenetrating, stress-free upper and lower boundaries. The details of the numerical algorithm used is described in the Appendix. Briefly, we use a mixed pseudo-spectral and finite-difference formulation, where the governing equations are Fourier analyzed in the two horizontal directions, and the vertical derivatives are written in the centered, fourth-order finite difference form. The equations are then time advanced using a semi-implicit method for which a second-order Adams-Bashforth scheme is used for the nonlinear advection terms and a second-order Crank-Nicholson scheme is applied for the diffusion terms.

For the simulations in this paper, the two horizontal dimensions of the Cartesian simulation box are of the same size L, and the vertical height of the box is $2L$, which spans 3.1 density scale heights. The ratio of density between the top and bottom is 0.05. A uniform grid of $128 \times 128 \times 256$ is used for the $L \times L \times 2L$ domain. The governing equations explicitly include viscosity (μ), magnetic diffusivity (η), and thermal diffusivity (K). In our simulations, we let μ, η, and $K\rho_0$ be constants in the domain. Like all numerical studies that are limited by the finite resolution of the simulation grid, the effective values of these diffusive parameters are generally much greater than what are expected under solar conditions. Hence, the interpretation of the numerical results will be subject to the uncertainties of the effects of the unresolved small-scale dynamics. The important nondimensional parameters in our numerical simulations are the viscous Lundquist number $S_v \equiv \rho_r v_{A0} a/\mu$, and the resistive Lundquist number $S_r \equiv v_{A0} a/\eta$, in which ρ_r is the density at the bottom of the domain, v_{A0} is the Alfvén speed at the axis of the initial flux tube, and a is the initial tube radius (defined in eq. [13] below). The values of S_v and S_r are, respectively, 43 and 4300. We use a large value of S_r (i.e., low resistivity) so that the flux "frozen in" condition (and

hence the topological constraint on the magnetic field) is satisfied as closely as possible, while the low value of S_v ensures that sharp velocity structures do not form. We set thermal diffusivity to a low value so that there is negligible heat diffusion across the flux tube during its evolution. We have done many tests to confirm the reliability of the code. One test is a comparison of the results of our code with that used in Linton et al. (1999), which is a fully compressible MHD code using very different numerical algorithms. We found that in the absence of gravity and stratification, our code produces results that are in good agreement (better than 3%) with that of Linton et al. (1999) on the nonlinear evolution of a kink unstable flux tube.

3. THE RELEVANT TIMESCALES OF THE PHYSICAL PROBLEM

The linear helical kink instability of a cylindrical, twisted magnetic flux tube has been studied extensively both in fusion plasma physics and in the context of solar physics (see, e.g., Linton et al. 1996 and the references therein). In this paper, we consider a uniformly twisted magnetic flux tube that has the form

$$\boldsymbol{B} = B_\theta(r)\hat{\theta} + B_x(r)\hat{x} \tag{12}$$

and

$$\begin{cases} B_x(r) = B_{x0} \exp\left(-r^2/a^2\right), \\ B_\theta(r) = \alpha r B_x(r), \end{cases} \tag{13}$$

where $\hat{x}$ is the tube axial direction, $\hat{\theta}$ is the azimuthal direction in the tube cross section, and r is the radial distance to the central axis. The constant α denotes the rate of field-line rotation about the central axis per unit length of the tube. In the ideal limit, this twisted flux tube is unstable to helical motion of the form $v(r) \exp[i(kx + \theta)]$, if α is above a critical value $\alpha_c = 1/a$. The linear growth rates for the unstable kink modes of the twisted flux tube can be computed by solving the Newcomb equation subject to the appropriate boundary conditions (see, e.g., Freidberg 1982; Linton et al. 1996). Figure 1 shows the ideal growth rates of the unstable helical kink modes, for two example cases with $\alpha = 4/a$ and $\alpha = 1.5/a$. In each case, there is a range of axial wavenumber k on either side of $k = -\alpha$ that is unstable.

The presence of finite viscosity and resistivity will change the growth rates from their ideal values (see, e.g., § 5.2 of Linton et al. 1998). In this work, we investigate only the long wavelength range of the unstable modes (with $|k| < \alpha$) which are less affected by the presence of dissipation. For our numerical simulations, the most important dissipative effect is the viscosity, which reduces the growth rates of the unstable kink modes and increases the critical value of α for the onset of instability. Through direct numerical simulations of the kink instability (in the absence of gravity and stratification), we found that the peak growth rate Ω (in units of v_{A0}/a) of the unstable kink modes (in the range of $|k| < \alpha$) is reduced from the ideal value of about 1.67 to 1.4 in the case of $\alpha = 4/a$, and from about 0.2 to 0.11 in the case of $\alpha = 1.5/a$. Furthermore, we found that the critical value of α for the onset of kink instability is increased to about $1.28/a$ (rather than the ideal value $\alpha_c = 1/a$).

The rise time of a magnetic flux tube through the convection zone is estimated to be $\tau_{\rm rise} \sim H_p/v_{\rm rise}$, where H_p is the pressure scale height and the rise velocity $v_{\rm rise} \sim (a/H_p)^{1/2} v_{A0}$ (Parker 1975). Let the radius of the flux tube $a \sim 0.1H_p$, then $\tau_{\rm rise} \sim 30(a/v_{A0})$. If the rise time $\tau_{\rm rise}$ is longer than the e-folding growth time $\tau_{\rm min}$ for the fastest growing kink mode, then the flux tube is expected to become kinked during the rise. The e-folding time decreases with increasing $\alpha^2 - \alpha_c^2$ (see Linton et al. 1996). For the cases of $\alpha = 4/a$ and $1.5/a$, $\tau_{\rm min} = 0.71a/v_{A0}$ and $9a/v_{A0}$, respectively (including the effect of viscosity). Both are small compared to $\tau_{\rm rise}$. We find that $\tau_{\rm min}$ becomes comparable to $\tau_{\rm rise}$ when $\alpha \approx 1.34/a$. Therefore, one can expect to see significant kinking of the tube axis during its rise if the initial α is greater than $1.34/a$. Furthermore, it has been argued (Parker 1979, chap. 9; Linton et al. 1996; Emonet & Moreno-Insertis 1998) that as a horizontal flux tube rises and expands, the longitudinal field decreases at a faster rate ($B_x \propto R^{-2}$, with R being the tube radius) than the transverse field ($B_\theta \propto R^{-1}$), making the tube more kink unstable. Previous two-dimensional simulations of the rise of twisted, horizontal flux tubes (see, e.g., Moreno-Insertis & Emonet 1996; Fan et al. 1998a), show that the tube cross section does not maintain a circular shape as it rises. First, in order for the flux tube cross section to withstand the distortion by the hydrodynamic forces and rise cohesively, the Alfvén speed of the transverse magnetic field in the tube cross section needs to be at least comparable to the rise velocity

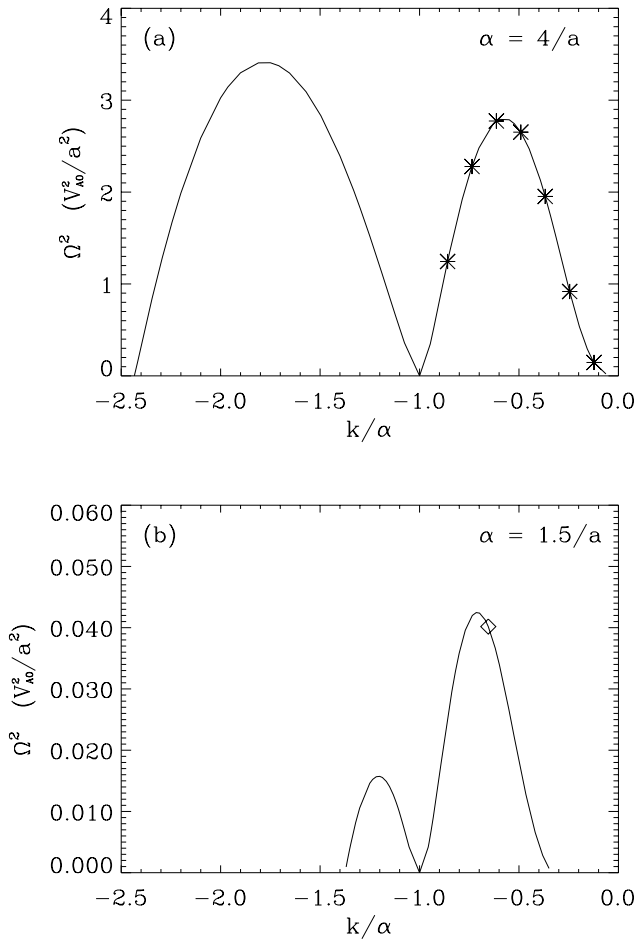

FIG. 1.—Linear growth rate Ω of unstable helical kink motion as a function of axial wavenumber k for a twisted magnetic flux tube described by eq. (13), with $\alpha = 4/a$ (*a*), and $\alpha = 1.5/a$ (*b*). In the case with $\alpha = 4/a$, the asterisks (*) correspond to wavenumbers $k_j = 2\pi j/L$, where $j = 1, 2, 3, 4, 5, 6$, and 7, and L is the length of the flux tube in the simulation box. In the case with $\alpha = 1.5/a$, the diamond corresponds to wavenumber $k_2 = 2\pi(2/L)$.

$v_{\rm rise}$ of the tube. This leads to a minimum twist for the flux tube: $\alpha_{\rm min} \sim (a/H_p)^{1/2} a^{-1} \sim 0.3/a$. Even if the tube is sufficiently twisted ($\alpha > \alpha_{\rm min}$) to maintain a cohesive rise, the tube cross section during the rise still deviates significantly from its initial circular profile. The cross section is flattened in the vertical direction and a layer of enhanced transverse field is developed at the boundary of the tube cross section (e.g., Emonet & Moreno-Insertis 1998; Fan et al. 1998a). Hence, the evolution of the kink instability of the flux tube may be quite different from that expected based on a simple self-similar expansion of the tube which maintains the form of its initial cylindrically symmetric cross-sectional profile. We therefore use our anelastic code to simulate the kink evolution of flux tubes which are rising and being distorted by hydrodynamical forces. We perform a series of simulations that cover a range of initial α-values (from $\alpha = 0$ to $\alpha = 4/a$) to see how the kink development of the rising tubes depends upon the initial twist.

4. SIMULATION RESULTS

4.1. *Initial Conditions*

For our numerical simulations, the initial cylindrical magnetic flux tube is given by equation (13). Figure 2 illustrates the cross-sectional profiles of the axial and azimuthal magnetic field of the tube in the case of very large twist with $\alpha = 4/a$. For all the simulations, the initial flux tube has the same axial field $B_x(r)$, and α is the parameter that varies. Hence, the magnitude of the azimuthal field B_θ is different. The flux tube sits initially at a height of about $\frac{1}{5}$ of the total height of the simulation domain, and the initial radius a of the tube is 0.085 times the pressure scale height at the bottom. Such a flux tube in a gravitationally stratified layer has a mechanical equilibrium state in which the density difference between the tube and the external medium, ρ_1, is zero, so that the buoyancy force is zero, and the gradient from the pressure perturbation p_1 balances the magnetic forces: $-\nabla p_1 + (1/4\pi)(\boldsymbol{B}\cdot\nabla)\boldsymbol{B} - \nabla(B^2/8\pi) = 0$. The equilibrium state of the entropy difference s_1 (between the tube and the external fluid) can then be calculated from p_1 and ρ_1 using equation (A3).

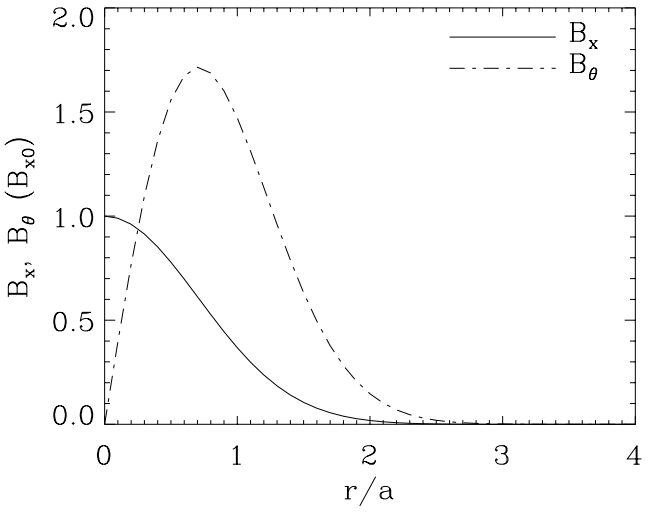

FIG. 2.—Variation of axial field strength B_x and azimuthal field strength B_θ with radius r in the initial tube cross section as described by eq. (13) with $\alpha = 4/a$.

To set the flux tube in motion, we make it buoyant by adding an entropy perturbation (equivalent to heating) to the above mechanical equilibrium state of the tube:

$$s' = s'_0(r) + \sum_{k_j} s'_{k_j}(r) \cos(k_j x + \phi_j) . \quad (14)$$

The pressure p_1 and density ρ_1 then adjust accordingly based on equation (A3) and the requirement that $\nabla\cdot(\rho_0 \boldsymbol{v}) = 0$ for the subsequent motion. The result is that ρ_1 is decreased and the flux tube becomes buoyant. The entropy perturbation contains a component $s'_0(r)$ that is constant along the tube axis (x-direction) and a set of components that vary sinusoidally along the axis with wavenumbers $k_j = 2\pi j/L$, where L is the length of the flux tube and $j = 1, 2, 3, 4, 5, 6, 7$. In the case with $\alpha = 4/a$, these wavenumbers k_j correspond to the asterisks in Figure 1*a* and are all kink unstable. In the case with $\alpha = 1.5/a$, only k_2 (see the diamond point in Fig. 1*b*) is within the $|k| < \alpha$ side of the unstable region. The profiles of $s'_0(r)$ and $s'_{k_j}(r)$ are Gaussians [$\propto \exp(-r^2/a^2)$], with the peak amplitudes of $s'_{k_j}(r) \propto 1/k_j$, and are all much smaller than the peak amplitude of $s'_0(r)$. [The amplitude of the largest $s'_{k_j}(r)$ is 0.025 of that of $s'_0(r)$.] The phases ϕ_j of each k_j modes are such that they all add constructively, i.e., $k_j x + \phi_j = 0$, at the middle cross section of the tube. The resultant buoyancy acceleration along the central axis of the tube is shown in Figure 3. The buoyancy acceleration is shown in unit of $B_{x0}^2/4\pi H_r \rho_r$, where H_r and ρ_r are, respectively, the pressure scale height and density at the bottom of the domain. In each tube cross section, the buoyancy acceleration decreases with r from the value on the axis, following a Gaussian profile. The mean buoyancy acceleration of the tube, as calculated by averaging over the volume where the field strength is above 10% of the peak field strength, is $0.25 B_{x0}^2/4\pi H_r \rho_r$. As a comparison, a thin flux tube in pressure and thermal equilibrium with its surrounding has a buoyancy acceleration that is equal to $B_{x0}^2/8\pi H_r \rho_r$. The peak buoyancy acceleration at the axis of the initial tube is thus about 2 times the isothermal thin tube value, and the mean buoyancy acceleration of the initial tube cross section is about a half of the thin tube value. The mean buoyancy of the entire tube (resulting from the s'_0 component) will cause the tube to rise as a whole. The small variation of buoyancy along the tube axis will drive planar undulation of the flux tube. Each sinusoidal undulating mode can be decomposed into two helical kink modes of opposite handedness. The kink mode with the same handedness as that of the field line twist will be excited if the twist is sufficiently high for the onset of the instability. For all cases studied in this paper, the initial buoyancy of the flux tube is the same.

4.2. *Overview of Final Configurations*

In Figure 4, we show the final magnetic flux tubes resulting from several simulations with different values of α. The top two rows of images show the volume rendering of the absolute magnetic field strength ($|B|$) of the final flux tubes, as viewed from two different perspectives. Each volume pixel in the box is assigned a brightness and opacity based on the value of $|B|$ at that point. Larger (smaller) $|B|$ corresponds to brighter (darker) and more opaque (transparent) pixels. In the bottom two rows of panels, we plotted a characteristic field line of each of the final flux tubes. The field line shown is the one that goes through the Lagrangian element which was originally placed at the

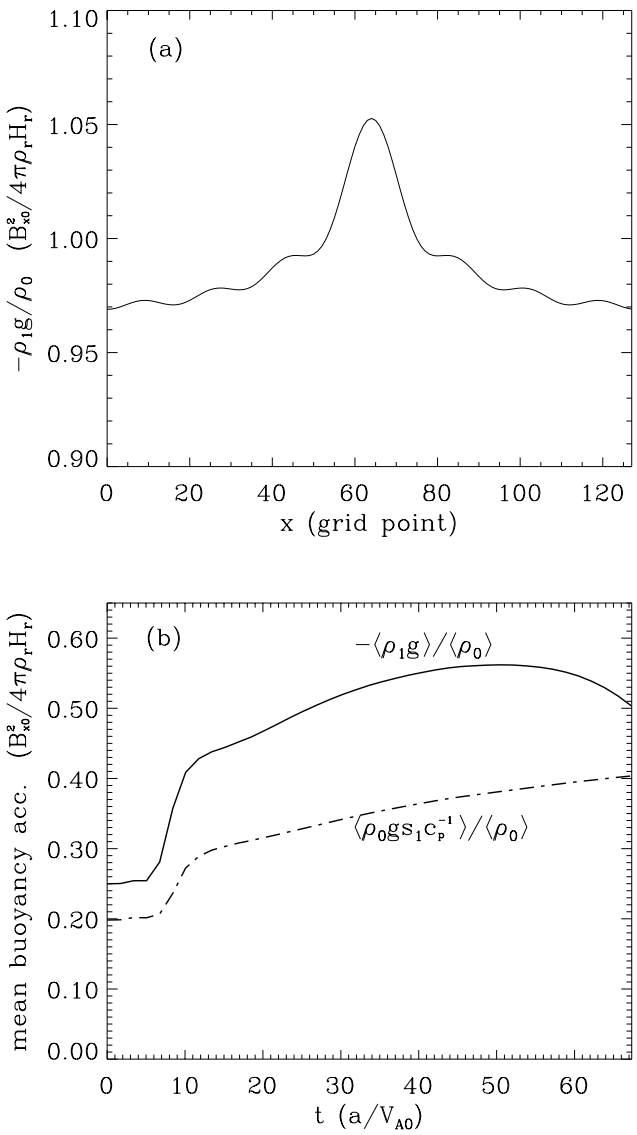

FIG. 3.—(*a*) Variation of initial buoyancy acceleration along the tube axis. (*b*) Evolution (in the case of $\alpha = 4/a$) of the mean buoyancy acceleration of the tube $-\langle\rho_1 g\rangle/\langle\rho_0\rangle$, in comparison with the evolution of $\langle\rho_0 g s_1 c_p^{-1}\rangle/\langle\rho_0\rangle$, which shows the contribution to the variation of buoyancy due to heating. Here angle brackets denote an average over the volume of the flux tube approximated by the region where the field strength is above 10% of the peak value. In both panels, the buoyancy acceleration is shown in unit of $B_{x0}^2/4\pi H_r \rho_r$, where B_{x0} is the field strength at the initial tube axis, H_r and ρ_r are, respectively, the pressure scale height and density at the bottom of the domain.

central point ($x = L/2$) of the initial tube axis and was followed during the evolution. In the ideal limit of zero resistivity, all the Lagrangian elements of the initial tube axis should remain on a single field line throughout the evolution. However, this is no longer true in the simulations due to the presence of finite magnetic diffusion and field-line reconnection. Nevertheless, due to the low resistivity, the field line shown in Figure 4 still roughly resembles the curve that connects the Lagrangian elements originated from the initial tube axis, and hence it reflects the amount of kinking the tube develops during the rise. We find from our simulations that for tubes with sufficiently supercritical twist ($\alpha > 1.34/a$) such that the *e*-folding time $\tau_{\rm min}$ for the growth of kink instability is small in comparison to the rise time $\tau_{\rm rise}$, the development of the kink instability during the rise can lead to large distortion of the tube, producing localized kinks where the tube orientation is changed by $\gtrsim 90°$ (see Figs. 4*a* and 4*b*). The amplitude of the kinking of the flux tube decreases with decreasing α. For the cases with initial twist that is near the ideal critical limit ($\alpha_c = 1/a$) for the onset of the kink instability, e.g., $\alpha = 1.2/a$ and $0.9/a$, the tubes become moderately kinked, with no sharp local bending of the tube axis (see Figs. 4*c* and 4*d*). When the initial twist of the tube is decreased to about $\alpha = 0.5/a$, which is significantly below α_c but sufficiently twisted ($\alpha > \alpha_{\rm min} \sim 0.3/a$) for maintaining a cohesive rise of the tube (Moreno-Insertis & Emonet 1996; Fan et al. 1998a), we find essentially no kinking of the tube axis (see Fig. 4*e*). Finally, if the initial flux tube is not twisted ($\alpha = 0$, this case not shown in Fig. 4), we find that the tube breaks up into two fragments which move apart horizontally and cease to rise, similar to what was found in previous two-dimensional simulations (Schüssler 1979; Longcope, Fisher, & Arendt 1996).

The length scale of the flux tubes being studied in these simulations is $L \approx H_r$, where H_r is the pressure scale height at the bottom. Hence, the undular Parker instability is not permitted because its critical wavelength is greater than $2\pi(2\gamma)^{1/2} \approx 11.5$ times the pressure scale height (Spruit & van Ballegooijen 1983). Our simulations therefore only investigate the local kinking of a small segment of straight tube, which may be considered as a portion (e.g., the apex segment) of a larger scale Ω loop. The arching seen in the flux tubes in Figure 4 is due to the local, nonlinear evolution of the kink instability. The additional arching and tilting of the tube that can result from the Ω loop structure is not included. To simulate simultaneously the structure of a large Ω loop resulting from, e.g., the Parker instability and also the local development of the kink instability is still not computationally feasible because of the large separation in length scales between the two instabilities.

4.3. *Kink Evolution of the Rising Tubes*

In this section, we first look closely at the case with $\alpha = 4/a$, for which sharp, localized kinking of the flux tube develops. Then in comparison, we discuss the kink evolution of tubes with smaller initial twist.

A sequence of snapshots of the rising flux tube during the evolution is shown in Figure 5 for the case of $\alpha = 4/a$. Like Figure 4, the first two rows of images show the volume rendering of the absolute magnetic field strength $|B|$ of the tube, and the field lines plotted in the bottom two rows of panels show approximately the Lagrangian evolution of the axial field line of the initial tube. The marked times are in units of the Alfvén crossing time $a/v_{\rm A0}$. As was noted in § 3, the linear calculation in the absence of gravity and stratification showed that the *e*-folding growth time $\tau_{\rm min}$ for the kink instability is smaller than the typical rise time of the flux tube if $\alpha > 1.34/a$. In the case of $\alpha = 4/a$, $\tau_{\rm min}$ is only $0.71a/v_{\rm A0}$ and the flux tube becomes kinked before it has risen any noticeable distance (see Fig. 5). The axis of the tube evolves into a helix as a result of the growth of multiple kink modes. The helix is of the same sense of handedness as the twisted field lines of the initial tube.

The top panel of Figure 6 shows (in the case of $\alpha = 4/a$) the evolution of the total magnetic and kinetic energies (E_m and E_k), normalized to the initial magnetic energy, and the evolution of the total magnetic helicity $H_m \equiv \int \boldsymbol{A} \cdot \boldsymbol{B}\, dV$ in the simulation domain V, where $\boldsymbol{A}$ is the vector potential.

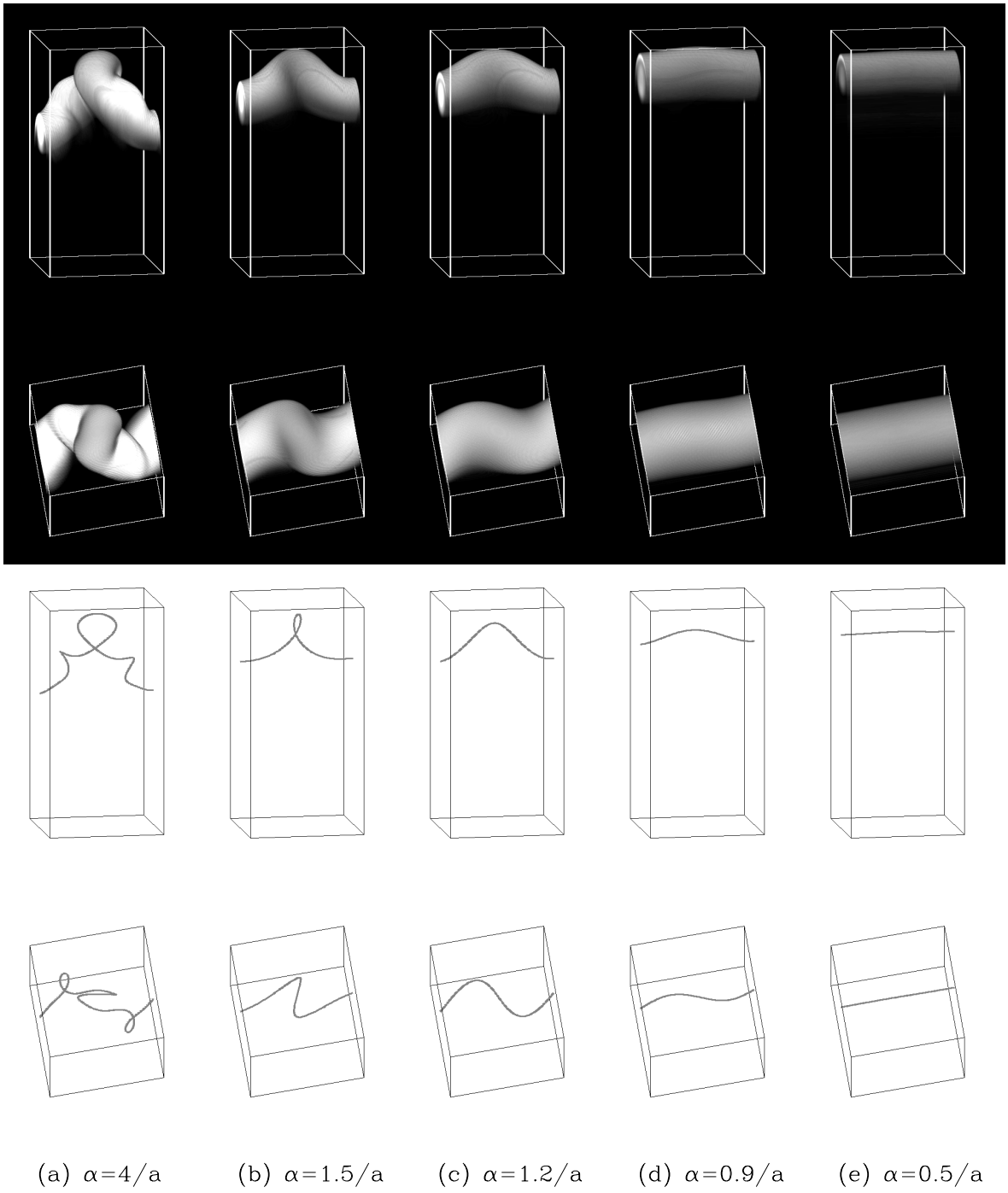

FIG. 4.—Final magnetic flux tubes resulting from several simulations with different values of α. The top two rows of images show the volume rendering of the absolute magnetic field strength ($|B|$) of the final flux tubes, as viewed from two different perspectives. Each volume pixel is assigned a brightness and opacity based on the value of $|B|$ at that point. Larger (smaller) $|B|$ corresponds to brighter (darker) and more opaque (transparent) pixels. A characteristic field line of each of the final flux tube is plotted in the bottom two rows of panels as viewed from two different perspectives. The field line plotted is the one that goes through the Lagrangian tracker which was originally placed at the central point ($x = L/2$) of the initial tube axis and was followed during the evolution.

According to the defining equations (A6), (A7), and (A8) for $\boldsymbol{B}$ in the Appendix, the corresponding $\boldsymbol{A}$ is given by

$$\boldsymbol{A} = \left[\frac{\partial \mathscr{B}}{\partial y} + \int_0^z \overline{B}_y(z')dz'\right]\hat{\boldsymbol{x}} + \left[-\frac{\partial \mathscr{B}}{\partial x} - \int_0^z \overline{B}_x(z')dz'\right]\hat{\boldsymbol{y}} + \mathscr{J}\hat{\boldsymbol{z}}\,, \qquad (15)$$

Where $\mathscr{B}(x, y, z)$, $\mathscr{J}(x, y, z)$, $\overline{B}_x(z)$, and $\overline{B}_y(z)$ are dependent variables being directly calculated in the simulations (see the description in the Appendix). The magnetic field $\boldsymbol{B}$ is zero at the upper and lower boundaries before the tube approaches the surface, and both $\boldsymbol{A}$ and $\boldsymbol{B}$ are periodic at the side boundaries. It can be shown that the total magnetic helicity H_m defined above is a conserved quantity in the ideal case of zero resistivity. In Figure 6, H_m is expressed in

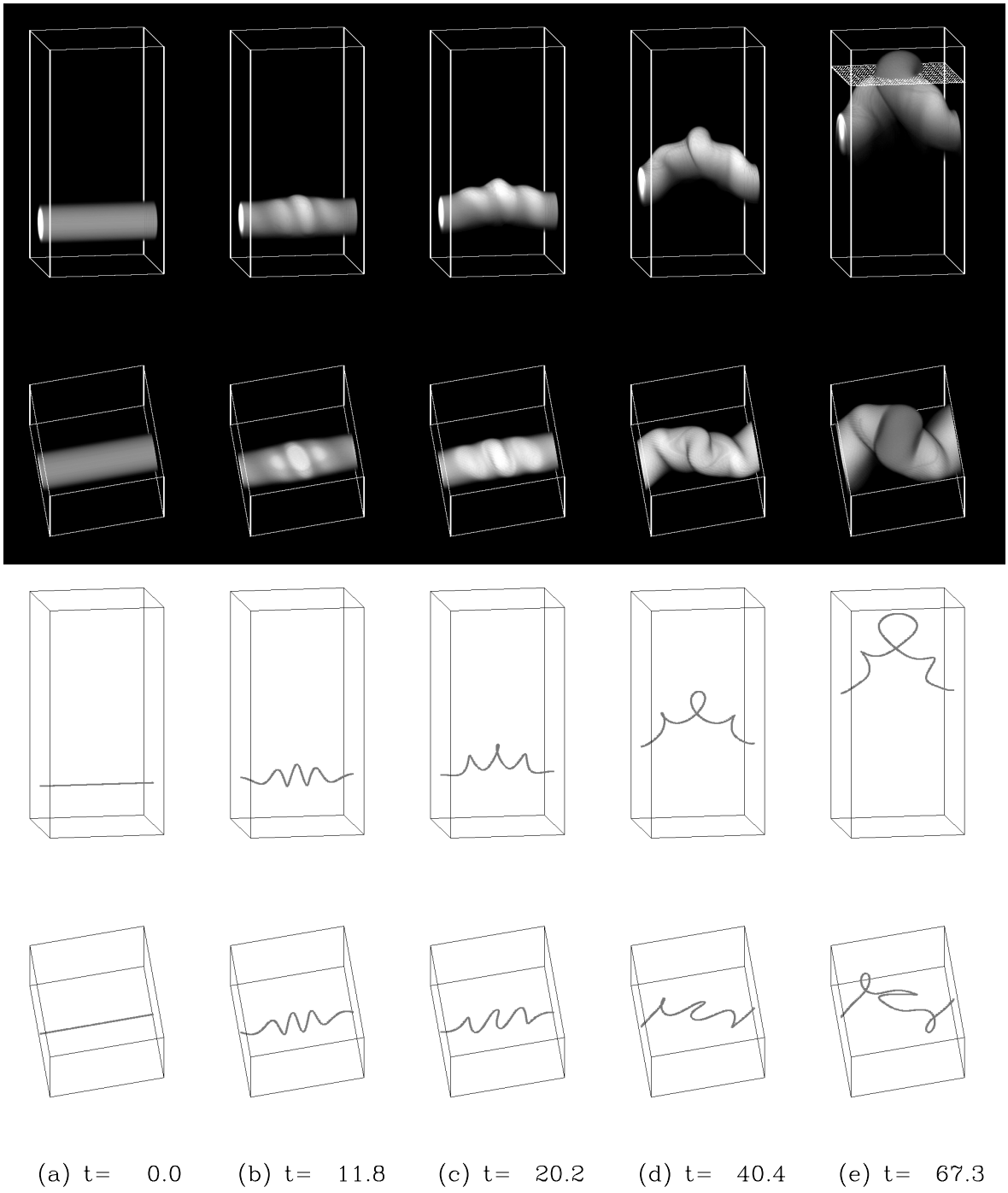

FIG. 5.—Sequence of snapshots of the rising flux tube during the evolution for the case with $\alpha = 4/a$. Like Fig. 4, the first two rows of images show the volume rendering of the absolute magnetic field strength $|B|$ of the tube, and the field lines plotted in the bottom two rows of panels show approximately the Lagrangian evolution of the axial field line of the initial tube. The marked times are in unit of the Alfvén crossing time a/v_{A0}.

units of Φ^2, where Φ is the total magnetic flux of the tube. H_m is initially equal to $(\alpha L/2\pi)\Phi^2 \approx 8.15\Phi^2$. The initial kink development (from $t = 0$ to roughly $t = 13a/v_{A0}$) is qualitatively similar to the kink evolution of flux tubes in the absence of gravity and stratification as described in Linton et al. (1998). The characteristic behavior during this stage is that the unstable kink modes first grow exponentially, and after the linear phase which lasts several Alfvén crossing times, the kink motion saturates as indicated by the first peak in E_k in the top panel of Figure 6. The kinking of the flux tube causes the magnetic energy to drop sharply while approximately conserving the magnetic helicity H_m. The decrease in magnetic energy partly goes to heating through direct Ohmic dissipation and is partly converted to the kinetic energy of the kink motion, which is then also converted to heat through viscous dissipation. After the kink saturates, the kinetic energy decreases. However, because of the presence of the driving buoyancy force, the flux tube does not settle into a stable kinked equilibrium as was found in Linton et al. (1998). After a brief decline the kinetic energy continues to increase steadily as a result of the buoyancy-driven acceleration of the tube, and the kink con-

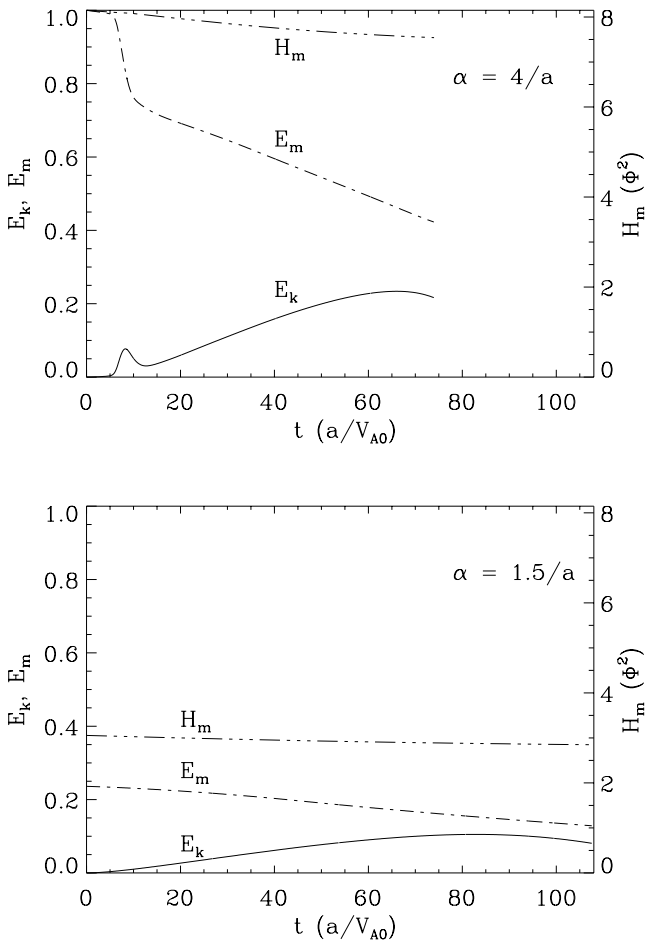

FIG. 6.—Evolution of the total magnetic and kinetic energies (E_m and E_k) and the evolution of the total magnetic helicity H_m in the cases with initial twist $\alpha = 4/a$ (*top*) and $\alpha = 1.5/a$ (*bottom*). The energies are all normalized to the initial magnetic energy of the tube with $\alpha = 4/a$. The magnetic helicity H_m is expressed in units of Φ^2, where Φ is the total magnetic flux of the tube.

tinues to develop as the tube expands and becomes more kink unstable (see the discussion in § 3).

The subsequent evolution of the tube can be described by its overall rise and a gradual arching and "buckling" of the kinked tube (see Figs. 5*c*, 5*d*, and 5*e*). The initial kink saturates because the tube has reached a quasi-equilibrium where the restoring tension from the writhing axial field has become strong enough to stop the kink growth. However, the weakening of the field as the tube rises upward into lower density region causes further distortion of the kinked tube. The up-down asymmetry resulting from gravitational stratification causes the kinked portions of the tube to protrude upward (hence, the overall arching of the tube) and rotate further away from the original orientation of the tube. This buckling deformation is most prominent at the apex of the tube. We can see that the final flux tube shape as outlined by the absolute field strength $|B|$ gives an apparent tube orientation at the apex that is about 120° away from the original $+x$ direction. The configuration of the final characteristic field line indicates that the Lagrangian segment at the middle of the initial tube axis has rotated clockwise by approximately 180° during the rise. Hence, we expect that the emergence of this buckled upper portion of the flux tube should give rise to a compact magnetic bipole with polarity orientation inverted from the Hale's polarity law. Figure 7 shows a horizontal cross section of the upper buckled portion of the flux tube at time $t = 67.2$. The height of the cross section is indicated by the dotted plane in the top panel of Fig. 5*e*. The solid (dotted) contours in Figure 7 represent the levels of positive (negative) B_z and the arrows show the horizontal field. We see a very tight bipolar structure with an apparent polarity orientation (i.e., the direction of the line drawn from the peak of the positive pole to the peak of the negative pole) rotated clockwise by about 145° from the $+x$ direction of the initial horizontal flux tube. The transverse (horizontal) field near the neutral line is sheared, although not as much as what is often observed in δ-spots where the transverse field runs nearly parallel to the neutral line.

The length scale over which the arching of the tube develops depends upon how the kink is distributed after the linear phase of the kink development. Therefore, it is certainly dependent upon the initial perturbation profile and also is affected by the periodic horizontal boundary conditions, which restrict the allowed wavelengths along the tube. We find that the upward arching (and the subsequent buckling) takes place over the region where the kinking is concentrated. We have done a simulation in which the horizontal size of the box in the direction of the tube is doubled (i.e., becomes $2L$). The initial perturbation profile is still given by equation (14) with all the modes (the number of modes is doubled) adding constructively at the middle cross section, resulting in a centrally peaked profile similar to that shown in Figure 3. The evolution in this case results in a final tube with a single main arch at the middle. The central arching is developed over a length scale of roughly L, where the kinking is concentrated. The resulting buckled configuration over the central L region is similar to that shown in

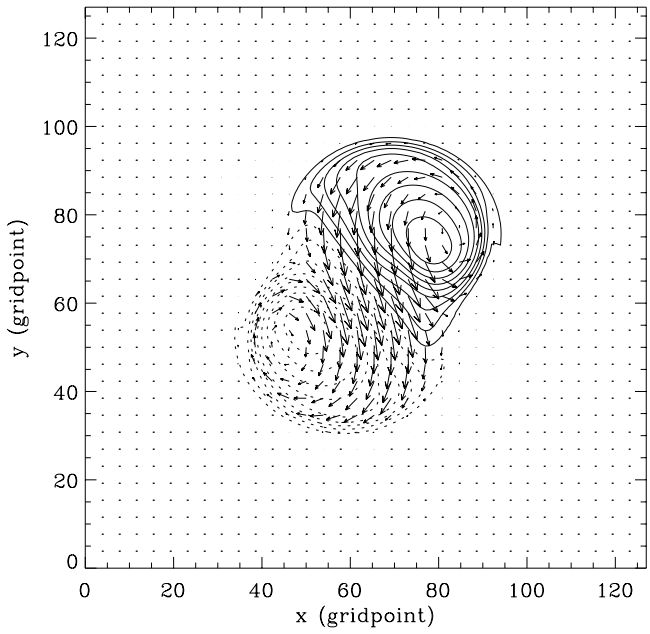

FIG. 7.—Horizontal cross section of the upper buckled portion of the final flux tube in the case with $\alpha = 4/a$. The height of the horizontal cross section is indicated by the dotted plane shown in the top panel of Fig. 5*e*. The contours denote the vertical magnetic field B_z with solid (dotted) contours representing positive (negative) B_z. The arrows show the horizontal magnetic field.

Figure 5. Hence, the restriction in the size of the domain to L in the tube direction has not significantly altered the evolution of the tube's shape.

In comparison to the case with $\alpha = 4/a$, the kink evolution in the case of $\alpha = 1.5/a$ is much more gradual because $\tau_{\min} = 9a/v_{A0}$ is about 10 times longer, and hence the separation of timescales between $\tau_{\min}$ and $\tau_{\rm rise}$ is less pronounced. Figure 8 shows a sequence of snapshots of the rising flux tube in the case of $\alpha = 1.5/a$. The flux tube first rises as a whole under the mean buoyancy, and the growth of the kink mode of wavenumber $k_2 = 2\pi(2/L)$ (the most unstable mode, see the diamond point in Fig. 1*b*) becomes apparent after the tube has risen a distance more than its own diameter. Subsequently, the flux tube arches and the apex portion distorts into a buckled configuration with the tube orientation being deflected clockwise by $\sim 90°$ from the initial $+x$ direction.

The bottom panel of Figure 6 shows the evolution of E_m, E_k, and H_m in this case. Note that the energies are still normalized to the initial E_m of the tube with $\alpha = 4/a$. We can see that the initial magnetic energy and the initial magnetic helicity $[(\alpha L/2\pi)\Phi^2 \approx 3.06\Phi^2]$ are both significantly smaller because of the smaller azimuthal field of the initial flux tube. The release of magnetic energy due to kinking is also much smaller and no longer stands out from the gradual decrease of magnetic energy resulting from the rise

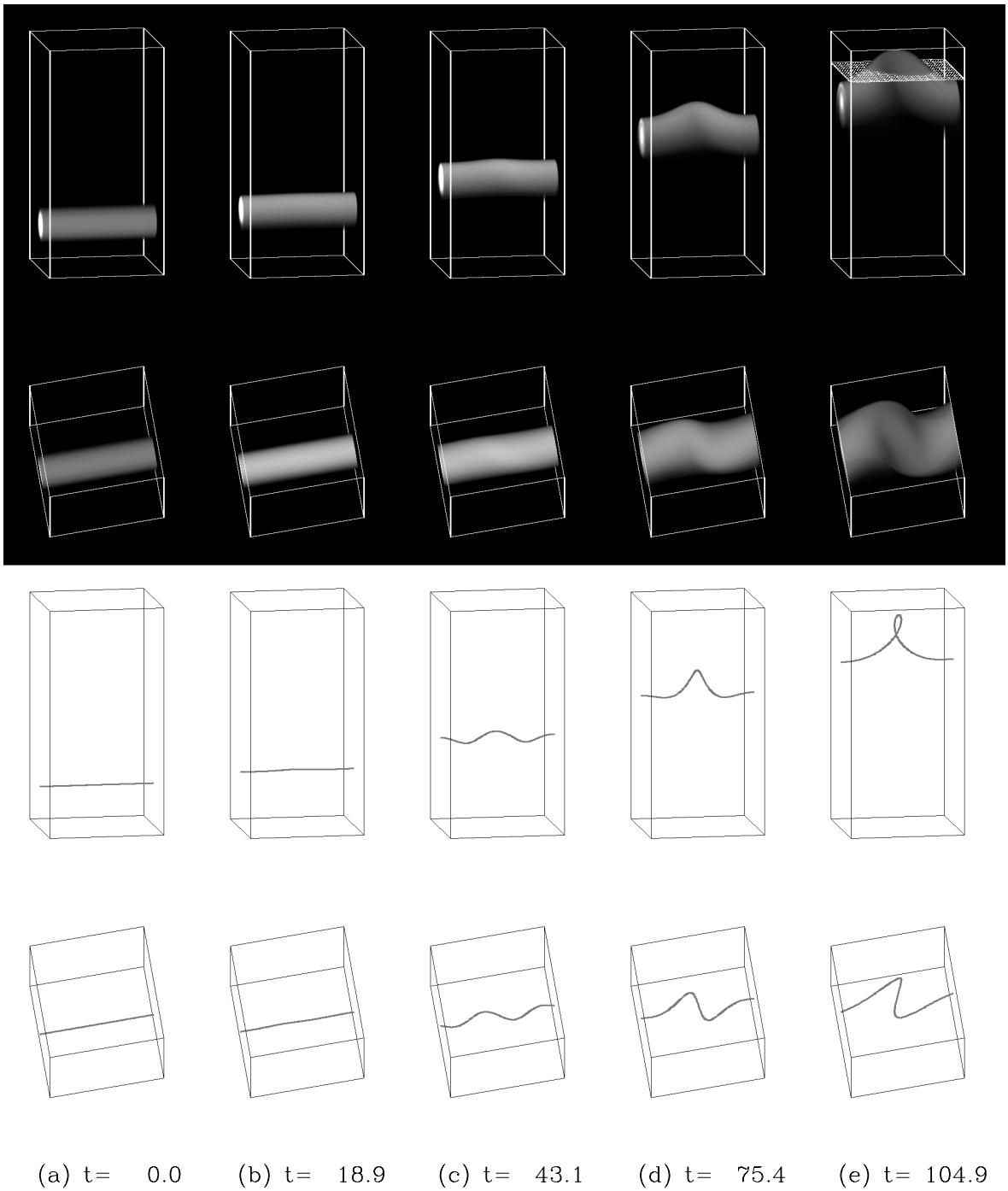

FIG. 8.—Same as Fig. 5, but for the case with $\alpha = 1.5/a$

and expansion of the flux tube. There is no distinct peak in the evolution of E_k that corresponds to the onset of the kink instability, in contrast with the case of $\alpha = 4/a$. Similar to the case of $\alpha = 4/a$, the total magnetic helicity H_m is approximately conserved. The total change of H_m is about 7% for both cases. This change is consistent with what is expected from the presence of finite resistivity, i.e., $dH_m/dt = -2\eta \int \boldsymbol{B} \cdot (\nabla \times \boldsymbol{B}) dV$, where V denotes volume.

Figure 9 shows a horizontal cross section of the upper buckled portion of the final flux tube in the case of $\alpha = 1.5/a$. The cross-sectional plane is indicated by the dotted plane in the top panel of Figure 8*e*. The magnetic field in the horizontal cross section appears as a compact bipolar region with the apparent polarity orientation (i.e., the direction from the peak of the positive polarity to the peak of the negative polarity) being approximately 90° away from the $+x$ direction, and with sheared transverse field near the polarity inversion line. At the end of our simulation, the flux tube is still entirely submerged beneath the surface in a pressure-dominated plasma and is not yet significantly affected by the impenetrable upper boundary. The emergence of the flux tube through the surface into the low-β plasma of the atmosphere is a complicated dynamical process that is beyond the scope of the current model. Hence, the cross-sectional structures shown in Figures 7 and 9 do not correspond directly to the observed photospheric magnetograms. Our present calculations are aimed only at studying the flux tube configurations that can be produced from the nonlinear kink evolution during the rise through the solar convection zone. Nevertheless, it is still interesting to note the morphological similarities between the cross-sectional magnetic field shown in Figures 7 and 9 and that of δ-configuration sunspots (see further discussion in § 5).

As the initial twist (α) of the flux tube decreases further from $\alpha = 1.5/a$, the kinking of the tube also becomes milder. In the cases with $\alpha = 1.2/a$ and $0.9/a$ (see Figs. 4*c* and 4*d*), we find that the kink development only results in smooth undulation of the tube, as can be seen from the Lagrangian evolution of the initial tube axis. The initial flux tubes in these two cases are stable against kinking based on the simulations in a uniform fluid without buoyancy and stratification (including the effect of viscosity). However, the tube is subsequently made kink unstable as it rises and expands, because the longitudinal field decreases at a faster rate than the azimuthal field. The flux tube axis develops significant kinking, with the kink mode of the lowest wavenumber $k_1 = 2\pi/L$ being the dominant mode. On the other hand, when the initial twist is decreased to $\alpha = 0.5/a$ (which is 50% of α_c), no kinking of the flux tube is excited during the rise (see Fig. 4*e*). There is a tiny amount of bending of the tube axis (hard to see in Fig. 4*e*) which can be accounted for by the small variation of initial buoyancy along the tube.

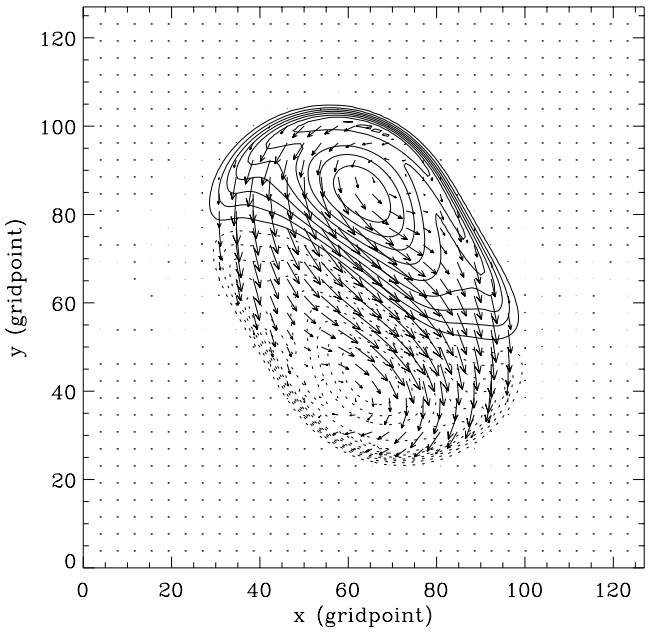

FIG. 9.—Same as Fig. 7, but for the case with $\alpha = 1.5/a$. The height of the horizontal cross section is indicated by the dotted plane shown in the top panel of Fig. 8*e*.

4.4. *Evolution of Field Strength and Rise Velocity*

The upper panel of Figure 10 shows the evolution of magnetic field strength at the tube apex as a function of height. It is determined by following the field strength at the apex of the characteristic field line which corresponds to the Lagrangian evolution of the initial tube axis. Several cases with different initial twist are shown. For comparison, the dotted line in Figure 10 shows the variation of the axial field strength B of a thin, horizontal (unkinked) flux tube with height, which is simply described by $B \propto 1/\rho_0$, where ρ_0 is the fluid density. The growth of the kink instability causes writhing of the initially straight axial field line into a helix (see, e.g., the bottom two rows of panels in Figs. 5 and 8). This results in stretching of the field line and increases the field strength along it. In the case with the largest initial twist ($\alpha = 4/a$), we see a substantial increase of the axial field strength (about 40%) due to the initial rapid growth of the kink instability. In the subsequent evolution, the field strength at the apex remains greater than that expected from the rise of a thin, horizontal flux tube. For tubes with less initial twist, the amplitude of kinking of the tube and the enhancement of axial field strength due to kinking both become less significant as can be seen in the upper panel of Figure 10. In the case with $\alpha = 0.5/a$, where no significant kinking of the tube is seen during the rise, the evolution of the tube axial field strength essentially follows the variation of $B \propto 1/\rho_0$.

The lower panel of Figure 10 shows the magnetic field strength along the characteristic field line (shown in Fig. 5) at several different instances during the evolution of the tube with $\alpha = 4/a$. For comparison, the field strength along the initial tube axis is shown as the dotted line. The curves for $t = 8.4$ and $t = 11.8$ (corresponding to Fig. 5*b*) show that the stretching is taking place along the entire tube, not just at the apex; the field strength along the entire field line is increased in comparison to the initial axial field. Although the axial field increases as a result of the writhing of the tube axis, the total magnetic energy decreases sharply during the kink development because of the decrease in the azimuthal field. This behavior of the axial and azimuthal fields, and the magnetic energy as a result of kinking, has been explained analytically in Linton et al. (1999, § 4.1), using a simplified model which assumes that the cylindrical flux tube is kinked into a helical shape by displacement of tube cross sections without changing their circular cross-sectional profile. Both the increase in the axial field and the decrease in the azimuthal field resulting from kinking of the

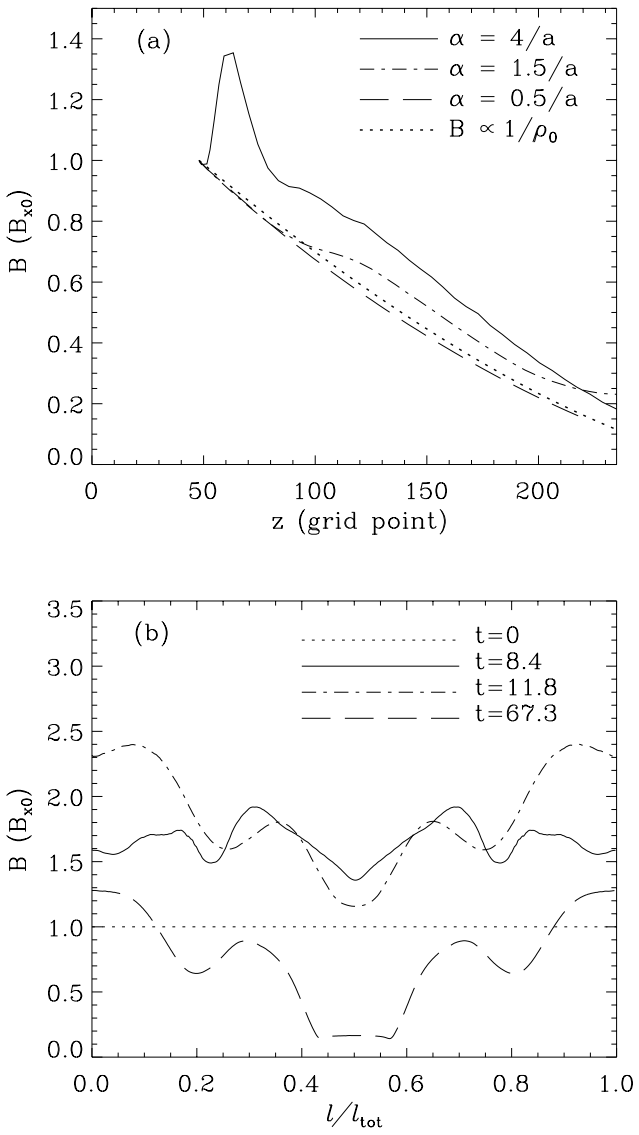

FIG. 10.—(*a*) Evolution of magnetic field strength B at the tube apex as a function of height for several cases with different initial twist. The field strength is determined at the apex of the characteristic field line, which corresponds to the Lagrangian evolution of the initial tube axis. In comparison the dotted line corresponds to $B \propto 1/\rho$, which describes how the axial field strength of a thin, horizontal (unkinked) flux tube is expected to vary with height. (*b*) Magnetic field strength along the characteristic field line at several different instances during the evolution of the tube with $\alpha = 4/a$. For the horizontal axis, l is the arc length along the field line and l_{tot} is the total length of the field line.

tube will decrease the plasma pressure in the tube and will consequently increase the tube buoyancy. (Decreasing the azimuthal field will lead to a lower plasma pressure at the tube axis because of the reduction in the confining force by the tension of the azimuthal field.) Furthermore, heating caused by the dissipation of magnetic and kinetic energy during the kink development also enhances the buoyancy of the tube. The latter contribution due to heating may be largely artificial because of the much higher viscosity and resistivity in the simulations than their realistic solar values (see further discussion of this in § 5). Figure 3*b* shows the evolution of the mean buoyancy acceleration of the tube $-\langle \rho_1 g \rangle / \langle \rho_0 \rangle$, where angle brackets denote an average over the volume of the flux tube approximated by the region where the field strength is above 10% of the peak value, for the case with $\alpha = 4/a$. For comparison, we also plotted the evolution of $\langle \rho_0 g s_1 c_p^{-1} \rangle / \langle \rho_0 \rangle$, which shows the contribution to the variation of buoyancy due to heating, i.e., due to the changes of the entropy in the tube. We do find a substantial increase in buoyancy as a result of kinking of the tube. From $t = 0$ to $t = 15$, the mean buoyancy acceleration has increased to about 1.8 times the initial value. About half of the increase is produced by heating, i.e., contributed from the increase in $\langle \rho_0 g s_1 c_p^{-1} \rangle / \langle \rho_0 \rangle$.

Figure 11 shows the evolution of the rise velocity of the flux tube as a function of time, for several cases with different initial twist. The upper panel shows v_z at the apex of the characteristic field line, and the bottom panel shows the mean vertical velocity $\bar{v}_z$ averaged over this field line. Because the initial buoyancy is set identically in all cases, the initial acceleration of the tube is the same. The initial value of $d\bar{v}_z/dt$ is approximately equal to the averaged value of $-\rho_1 g/2\rho_0$ over the initial tube axis, and the initial value of dv_z/dt for the apex is approximately equal to $-\rho_1 g/2\rho_0$ at the middle of the tube axis. Here $2\rho_0$ corresponds to the enhanced inertia experienced by the flux tube (Lamb 1945,

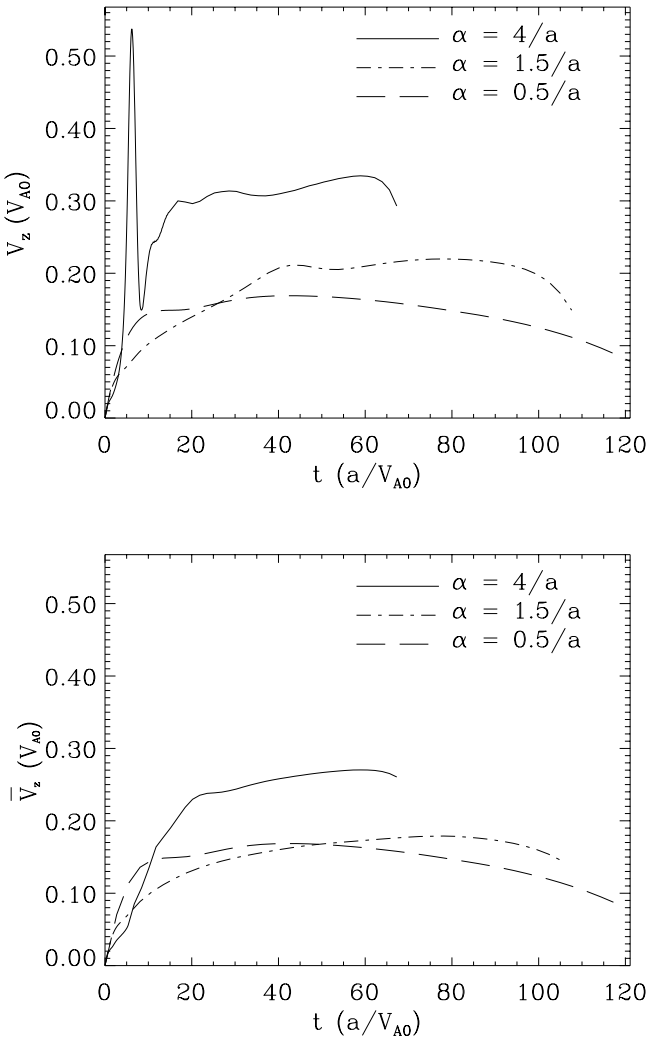

FIG. 11.—Evolution of the rise velocity of the flux tube as a function of time, for several cases with different initial twist. The upper panel shows v_z at the apex of the characteristic field line, and the bottom panel shows the mean vertical velocity $\bar{v}_z$ averaged over this field line.

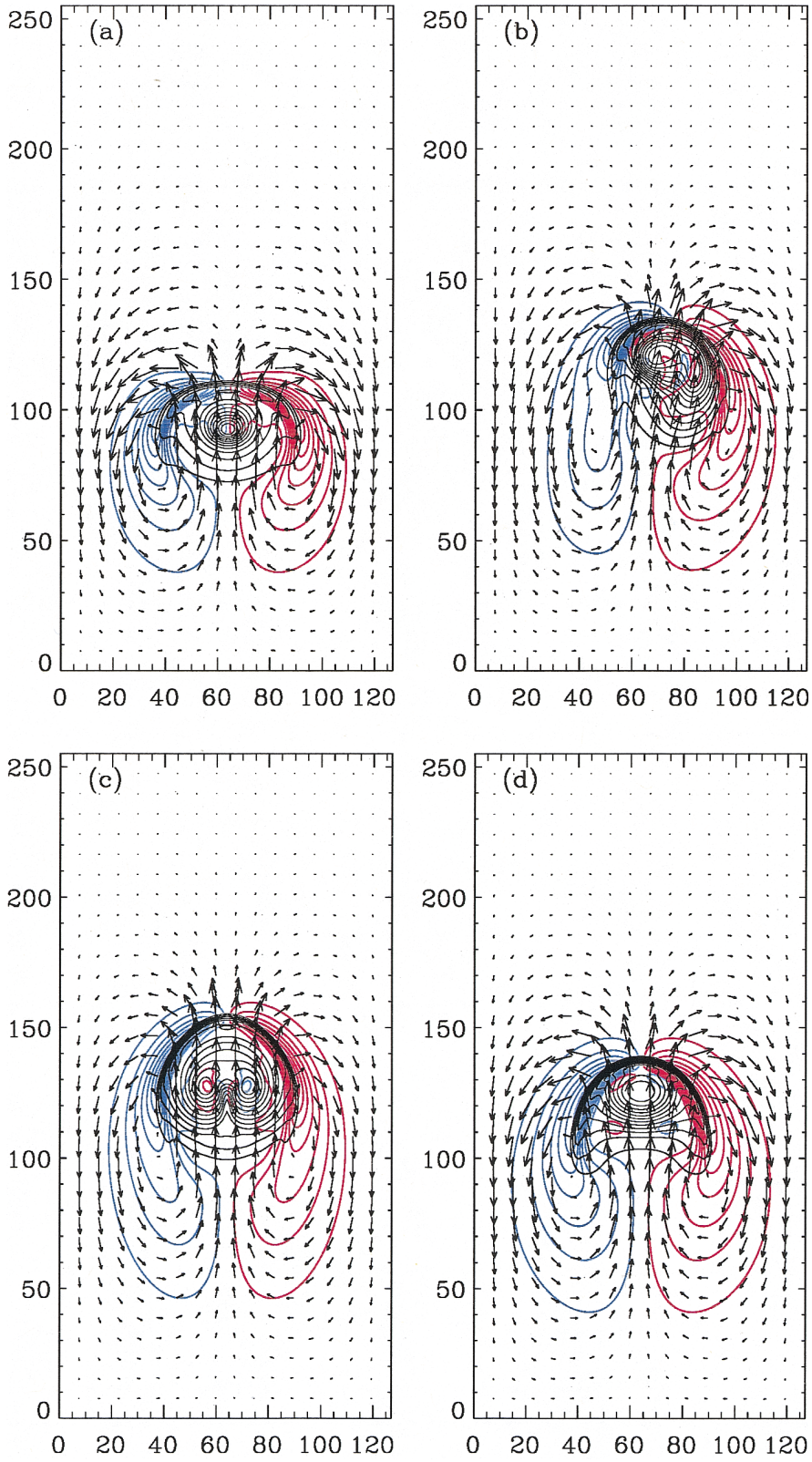

FIG. 12.—(*a*, *b*, *c*) Three different cross sections of the flux tube with initial $\alpha = 4/a$, at time $t = 40.4$. The cross sections are taken at (*a*) $x = 0$, (*b*) $x = L/4$, and (*c*) $x = L/2$, respectively. (*d*) Middle cross section ($x = L/2$) of the flux tube with initial $\alpha = 0.5/a$, at time $t = 52.4$. The arrows show the velocity field within the cross-sectional plane, the black contours indicate the magnetic field strength $|B|$, and the blue and red contours show the x component of the vorticity, with red corresponding to vorticity directing into the plane.

p. 76). Subsequently, the different amount of twist in the tubes causes their rise velocity to evolve differently. As described in § 3, the initial buoyancy decreases with r from the tube axis, so the central core of the tube is more buoyant. The faster acceleration of the core of the tube distorts the tube cross section, and the tube axis then experiences a restoring force from the azimuthal field. This back-reaction is greater for tubes with larger initial twist. Hence,

for a brief period after the beginning, the mean rise velocity of the axis $\overline{v}_z$ in the case with $\alpha = 4/a$ becomes slower than the other cases with smaller initial twist. However, the rapid kink development in the case of $\alpha = 4/a$ (as is evident from the spike in the evolution of apex v_z) increases the tube buoyancy (see Fig. 3*b*) and accelerates the overall rise of the tube to a roughly steady velocity (as represented by the steady phase of $\overline{v}_z$) that is larger than all the other cases. The enhancement of buoyancy due to kinking decreases with decreasing twist. For $\alpha = 0.5/a$, there is no significant kink development, and the evolution of the averaged $\overline{v}_z$ and the apex v_z are nearly identical (Fig. 11, *long-dashed lines*). The rise of the tube in this case is similar to what was found in previous two-dimensional simulations of the rise of twisted, horizontal flux tubes (Moreno-Insertis & Emonet 1996; Fan et al. 1998a; Emonet & Moreno-Insertis 1998). However, we note that our present three-dimensional simulations are in a much more viscous regime in comparison to the two-dimensional simulations. The Reynolds number for the flux tubes as estimated from the steady rise velocity, the radius of the tube, and the viscosity, is only ~ 10, more than an order of magnitude smaller than that in Fan et al. (1998a). By considering a balance of the mean buoyancy and drag in the steady rise phase, we find an effective drag coefficient C_D of about 3 for the tubes. This value of C_D is consistent with that found for a circular cylinder moving in a fluid at similar Reynolds numbers (see Batchelor 1967, p. 261).

Figures 12*a*, 12*b*, and 12*c* show the flow structure in three different cross sections of the flux tube with initial $\alpha = 4/a$, at time $t = 40.4$. The cross sections are taken at $x = 0$, $x = L/4$, and $x = L/2$. Figure 12*d* shows the middle cross section ($x = L/2$) of the flux tube with initial $\alpha = 0.5/a$, at time $t = 52.4$. In the case of $\alpha = 0.5/a$, the flow is nearly two-dimensional and the middle cross section shown in Figure 12*d* is representative of all the other cross sections. The arrows show the velocity field within the cross-sectional plane, the black contours indicate the magnetic field strength $|B|$, and the blue and red contours show the x component of the vorticity, with red corresponding to vorticity directing into the plane. As can be seen from the distribution of vorticity, the flow shown here is much more viscous in comparison to that obtained in the previous two-dimensional simulations. The thickness of the shear boundary layer at the two sides of the flux tube cross section is comparable to the radius of the tube. When we examine the flow field in the reference frame of the moving flux tube, we find that a region of two closed circulating eddies is barely discernible behind the tube during the steady rise phase in the case of $\alpha = 0.5/a$. However, for the rise of the tube with initial $\alpha = 4/a$, where the velocity field around the tube is more three-dimensional due to the kinking of the tube, we do not find noticeable structure of closed eddies behind the tube. It was found in the study of incompressible flow past a cylinder (see § 4.12 in Batchelor 1967) that a region of closed circulating fluid, consisting of two symmetric eddies, begins to form behind the cylinder as a result of advection of vorticity downstream when the Reynolds number is increased to 9. This suggests that the effective fluid Reynolds number for our current simulations is close to 9. The region of two closed eddies becomes longer and more prominent as the Reynolds number continues to increase, consistent with what was found in the two-dimensional simulations (Moreno-Insertis & Emonet 1996; Fan et al. 1998a). In the case of flow past a sphere (also § 4.12 in Batchelor 1967), the region of closed circulation behind the object begins to form at a higher Reynolds number, about 24.

5. DISCUSSION

Through three-dimensional numerical simulations, we have studied the nonlinear evolution of the kink instability of twisted flux tubes rising buoyantly through an adiabatically stratified layer. The length of the flux tube in our simulations is equal to the pressure scale height at the bottom of the layer. Hence, the development of the undular Parker instability is excluded because the minimum wavelength for the unstable modes is about 10 times that of the length of the simulated flux tube. Initial flux tubes sitting near the bottom of the layer are assumed to be uniformly twisted with the degree of twist measured by a parameter α, which is the angular rate of field-line rotation about the tube axis per unit length of the tube. We have performed a series of simulations with different initial twist ranging from $\alpha = 0$ to $\alpha = 4/a$, where a is the radius of the tube cross section defined in equation (13). We found from the simulations that in order for the flux tube to develop significant kinking during its rise through the layer, the initial twist of the tube needs to be close to or greater than the critical limit ($\alpha_c = 1/a$) for the onset of the kink instability. If the initial twist of the tube is too far below the critical limit (below about 50% of α_c), then there is no kink development and the evolution is similar to the results from previous two-dimensional simulations of the rise of twisted, horizontal flux tubes.

As noted by Parker (1979), the expansion of the twisted tube during its rise through the stratified layer makes the flux tube more kink unstable because of the faster decrease of the axial field strength in comparison to the azimuthal field strength. If we assume that the flux tube cross section expands self-similarly as the tube rises,

$$\begin{cases} B_x(r) = B_{x0}\, f\left(\dfrac{r}{a}\right) = B_{x0} \exp\left[-\left(\dfrac{r}{a}\right)^2\right], \\ B_\theta(r) = \alpha r B_x(r) = \alpha a B_{x0}\, \dfrac{r}{a} f\left(\dfrac{r}{a}\right), \end{cases} \tag{16}$$

where the profiles $f(r/a)$ and $(r/a)f(r/a)$ remain unchanged but the size scale a increases as the tube rises, then conservation of mass and of magnetic flux (both longitudinal and azimuthal) lead to $B_{x0} \propto \rho_0(z)$, and $\alpha_c = 1/a \propto [\rho_0(z)]^{1/2}$, while α remains constant. The enhancement of the kink instability is reflected in the decrease of α_c for fixed α. Linton et al. (1996) have derived an approximate scaling relation between the e-folding growth time $\tau_{\min}$ of the fastest growing kink mode and $\alpha^2 - \alpha_c^2$:

$$\tau_{\min} = C[v_{A0} R(\alpha^2 - \alpha_c^2)]^{-1}, \tag{17}$$

in which C is a constant, v_{A0} is the Alfvén speed at the tube axis and R is the tube radius, which we set equal to a. We let $C = 6.25$ so that for $\alpha = 1.5/a$, it gives the same value of $\tau_{\min}$ as that obtained from the linear calculation (see Fig. 1*b*). The height variation of v_{A0} follows $v_{A0} \propto [\rho_0(z)]^{1/2}$ based on the model of self-similar expansion. Using the scaling relation given in equation (17) we can estimate a total number of e-foldings N of the growth of the kink instability accumulated during the rise of the flux tube from its initial

height z_1 to the top of the layer z_2:

$$N = \int_{z_1}^{z_2} \tau_{\min}^{-1} v_r^{-1} \, dz \ , \tag{18}$$

where v_r is the rise velocity. In the region between z_1 and z_2, where α is below α_c, the integrand is set to zero. In calculating N, we assume that the flux tube is rising at a steady velocity v_r that is equal to $(a/H_p)^{1/2} v_{A0}$ evaluated at the initial height z_1. Figure 13 shows the result of N as a function of α obtained from the integration of equation (18). The result indicates that α needs to be above $0.65/a$ in order for the tube to go through at least one e-folding of the growth of the kink instability during the rise. Although the rising flux tube does not maintain a circular cross-sectional shape, this estimate based on the self-similar expansion of the tube helps to understand the simulation result of having essentially no kink development for the tubes with initial twist $\alpha \lesssim 0.5/a$.

On the other hand, our simulations show that if the initial twist of the tube is sufficiently supercritical that the e-folding time for the growth of the kink instability is small compared to the rise time of the tube, then sharp bending and distortion of the flux tube result from the nonlinear evolution of the kink instability. We find that the weakening of the flux tube field strength as it rises into fluid of decreasing density enhances the amplitude of kinking. The apex portion of the flux tube evolves into a buckled form with a local change of the tube orientation that exceeds 90°. The emergence of this buckled structure can give rise to a compact magnetic bipolar region with polarity order reversed from that expected from Hale's polarity law.

One interesting consequence of the development of the kink instability of the flux tube is that it enhances the buoyancy of the flux tube and speeds up the rise. The increase in buoyancy is caused by the writhing of the tube axis, which stretches the flux tube, and also caused by the heating of the tube due to the dissipation of magnetic and kinetic energy during the kink development. It is a concern that the substantial heating experienced by the flux tube may be an artifact of the low Reynolds numbers in the simulations. To test the effect of heating in the evolution of the tube, we repeated the simulation in the case of $\alpha = 4/a$, this time omitting the viscous and Ohmic heating terms in the energy equation so that the energy dissipation does not result in heating and therefore an increase in buoyancy. We find that the rise velocity in the steady rise phase is reduced to about 77% of the previous value, but it is still the fastest in comparison to other cases with smaller initial twist. The increase of buoyancy resulting from the initial rapid kink development is reduced to about a half of that obtained in the simulation with heating included. The final flux tube still evolves into the buckled configuration similar to that shown in Figure 5*e*, hence the buckling of the emerging flux tube does not depend on the effect of heating.

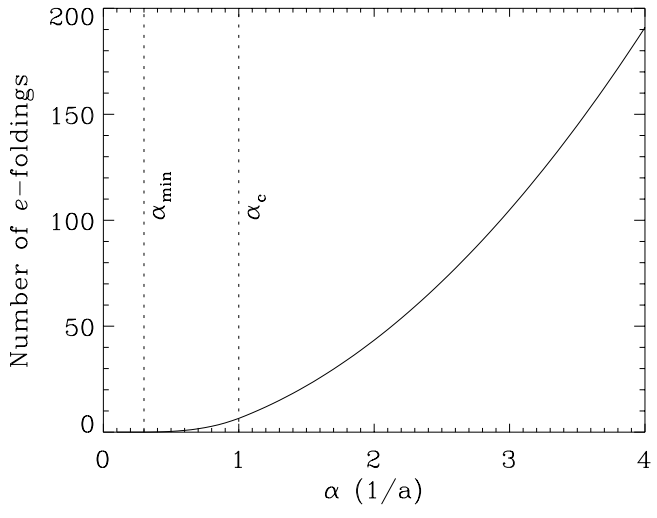

FIG. 13.—Number of e-foldings of the growth of the kink instability during the rise as a function of α, estimated from the integration of eq. (18). α_c indicates the critical twist (ideal value) for the onset of the kink instability, and $\alpha_{\min}$ indicates the minimum twist needed for the tube to rise cohesively.

As pointed out in § 4.3, there are many similarities between the magnetic field morphology shown in the horizontal cross sections of the upper buckled portion of the kinked flux tubes (Figs. 7 and 9) and that seen in δ-spots, for example, the reversed polarity order, the tightness of the bipolar pair, and the highly sheared transverse field at the neutral line (see, e.g., Zirin 1988, p. 336; Tanaka 1991; Leka et al. 1994). However, we have also found inconsistencies between the observed δ spots and the structure of the kinked flux tubes. One prediction from the theory of kinked flux tubes is that the sense of the writhe of the tube axis should be the same as that of the twist within the tube due to conservation of helicity (as noted in Leka et al. 1996; Linton et al. 1998). In our simulations, the flux tubes all have right-handed twist, and hence the writhe of the tube axis resulting from the kink instability is also right-handed. This leads to a clockwise rotation of the apex portion of the rising tube as viewed from the top. In the horizontal cross sections shown in Figures 7 and 9, the apparent polarity orientation of the bipolar structure is rotated clockwise by $\sim 145°$ and $\sim 90°$, respectively, from the $+x$ direction. This suggests that we can deduce from observations the sense of the writhe of the emerging Ω-loop from the tilt of the polarity orientation (i.e., the tilt of the line drawn from the f pole to the p pole of the bipolar region). A clockwise (counterclockwise) tilt from the east-west direction would correspond to a right-handed (left-handed) writhe of the Ω loop. The twist of the tube, on the other hand, can be deduced from J_z (vertical current) and B_z within each pole. We have examined several observed δ spots studied in Leka et al. (1994, 1996) and Lites et al. (1995), where vector magnetograms are provided, and found that not all of them obey the relation between twist and writhe as that required by a kinked tube. Leka et al. (1994, 1996) found that the polarity orientation of the δ spots in the active region NOAA 7260 in the northern hemisphere show a 90° counterclockwise tilt from the east-west direction, opposite to the tilt expected from the Joy's law. This suggests a left-handed writhe of the emerging Ω loop. The J_z and B_z determined from the vector magnetogram (Fig. 16 of Leka et al. 1994) indicate that the flux tube twist is also left-handed, consistent with what is expected for kinked tubes. However, in the case of the δ spot of NOAA 7201 studied by Lites et al. (1995), the relation between writhe and twist is not consistent with that of kinked flux tubes. The δ spot (see Fig. 1 in Lites & Low 1997), which is again in the northern hemisphere, show a polarity orientation that is tilted clockwise by about 90°, indicating a right-handed writhe of the Ω loop. On the other hand, the twist of the tube as determined from the vector magnetogram is left-handed, opposite to the

sense of the writhe. In Lites & Low (1997), the evolution of this δ spot is well explained by the emergence of a closed magnetic torus. Hence, active regions classified under the δ-configuration may not all originate from the emergence of kinked tubes. It is also possible that the large tilts seen in δ-spots are resulting from deformation by helical convective motions during the rise of the tube. This mechanism would produce a different kind of twist-writhe correlation for active regions based on helicity conservation (see Linton et al. 1998, § 2). However, it is doubtful if the helical convection would have enough force to produce the observed large tilts on rising Ω loops with superequipartition field strength. A statistical study of the twist-writhe relation of a large sample of δ spots will help to clarify how important a role the kink instability plays in the origin of these unusual active regions.

If indeed the majority of the δ spots observed on the solar surface are formed by the emergence of kinked flux tubes, then the results of our present simulations may give some indication of the twist of toroidal flux tubes at the base of the solar convection zone. Since only a small fraction of the observed active regions emerge as δ spots and show polarity orientations that are not in agreement with the Hale's polarity rule and the Joy's law, toroidal flux tubes in the solar interior must in general have twist that are well below the critical limit for the onset of the kink instability. What the typical amount of twist for most of the toroidal flux tubes is is still an open question, but preliminary studies (Longcope, Fisher, & Pevtsov 1998) indicate that most active region flux tubes have very small twist.

Our present simulations study the nonlinear kink evolution of a horizontal segment of rising flux tube which may be viewed as the apex portion of a larger Ω loop erupting through the solar convection zone. When the initial twist is sufficiently low ($\alpha \lesssim 0.5/a$) such that there is no development of the kink instability, then the rise of the flux tube is essentially uniform along the tube, similar to what was studied in the previous two-dimensional simulations (Moreno-Insertis & Emonet 1996; Fan et al. 1998a). As in the two-dimensional simulations, we still find that a minimum amount of twist ($\alpha_{\min} \sim 0.3/a$) is necessary for the tube to rise cohesively and carry most of its flux to the surface. We expect this result to change if we model instead the rise of the large-scale Ω loop resulting from the Parker instability. With the inclusion of the three-dimensional effect of the Ω loop, $\alpha_{\min}$ could be significantly smaller because of the nonuniform motion along the loop and the restoring force from the longitudinal magnetic field. Hence, the twist for most of the toroidal flux tubes at the base of the convection zone may be significantly below $\alpha_{\min}$. Because we are not simultaneously modeling the structure of the large-scale Ω loop resulting from the Parker instability together with the local development of the current driven kink instability, the effect of twist propagation along the Ω loop is not considered. Our present simulations show that the reversed polarity δ-configuration can be produced through the rise of flux tubes which are already highly kink unstable ($\alpha \gtrsim 1.5\alpha_c$) near the bottom of the convection zone. How some of the toroidal tubes obtain such a high amount of twist is unclear, but if the effect of the propagation of twist along the Ω loop is included, the initial twist needed for the toroidal flux tube to give rise to δ-spot regions may be reduced.

Finally, we comment on the effect of the Coriolis force due to solar rotation on the kink development of the rising flux tubes, which was not included in our simulations. By considering the Coriolis force as a small perturbation to the linearized momentum equation of the twist flux tube (in a uniform, incompressible fluid), we find that to first order, the Coriolis force does not affect the linear growth rate of the helical kink modes if the angular velocity of rotation is perpendicular to the tube axis, which corresponds to the case of a east-west oriented flux tube on the Sun. Hence, we expect that the Coriolis force to have little effect on the growth of kink modes with growth time significantly shorter than the rotation period (about a month). However, the influence of the Coriolis force may be significant for the evolution of kink modes with growth time comparable or longer than the rotation period, and it is expected to affect the buckling deformation found in the cases with $\alpha \gtrsim 1.5/a$ (see Figs. 5*c*, 5*d*, and 5*e*, and Figs. 8*d* and 8*e*). For the buckling deformation (as described in § 4.3), the kinked portions protrude upward into fluid of lower density and rotate. The sense of rotation depends on the sense of twist in the tube and is clockwise (counterclockwise) as viewed from the top if the twist is right-handed (left-handed). The Coriolis force, on the other hand, will also cause a rotation of the apex portion as it protrudes upward and expands due to the decrease in density. The rotation induced by the Coriolis force is hemisphere-dependent and is clockwise (counterclockwise) in the northern (southern) hemisphere. Hence, the Coriolis force will enhance (work against) the buckling deformation of a right-handed (left-handed) twisted tube in the northern hemisphere. Since the timescale over which the buckling develops is the rise time of the tube, which can be comparable to the rotation period, this asymmetric effect of the Coriolis force may be important. The influence of the Coriolis force and the simultaneous evolution of a rising Ω loop resulting from the undular Parker instability and the development of the kink instability on the loop will be topics of future investigations.

We thank Nic Brummell, Bob Kerr, and Steve Lantz for helpful advice on the numerical algorithms. We are grateful to Peter Gilman and an anonymous referee for reviewing the manuscript and for helpful comments. The numerical simulations are performed on the Cray J90 supercomputers of NCAR. This work has been supported by NSF grant AST 95-21779 and the NASA SPTP program.

APPENDIX A

THE NUMERICAL ALGORITHM

In this Appendix, we describe how we solve numerically the set of three-dimensional anelastic MHD equations (1)–(7) in a rectangular domain. To guarantee that the three-dimensional magnetic field $\boldsymbol{B}$ and momentum $\rho_0 \boldsymbol{v}$ are divergence free (eqs.

[2] and [4]), we write them in the form of vector potentials (see, e.g., Glatzmaier 1984):

$$\boldsymbol{B} = \boldsymbol{\nabla} \times \boldsymbol{\nabla} \times (\mathscr{B}\hat{z}) + \boldsymbol{\nabla} \times (\mathscr{J}\hat{z}) , \tag{A1}$$

$$\rho_0 \boldsymbol{v} = \boldsymbol{\nabla} \times \boldsymbol{\nabla} \times (\mathscr{W}\hat{z}) + \boldsymbol{\nabla} \times (\mathscr{Z}\hat{z}) , \tag{A2}$$

where $\hat{z}$ is the unit vector of the vertical direction and $\mathscr{B}$, $\mathscr{J}$, $\mathscr{W}$, and $\mathscr{Z}$ are spatially functions of (x, y, z). Thus, equations (1) and (4) are automatically satisfied. Furthermore, combining equations (6) and (7) to eliminate T_1, and using the conditions of adiabatic stratification and hydrostatic equilibrium for the background reference state, we obtain

$$\frac{\rho_1}{\rho_0} = \frac{p_1}{\rho_0 g h_0} - \frac{s_1}{c_p} , \tag{A3}$$

where $h_0 \equiv = -\rho_0 (d\rho_0/dz)^{-1}$ is the density scale height. Using equation (A3) to eliminate ρ_1 in equation (2), the momentum equation can be rewritten as

$$\frac{\partial \boldsymbol{v}}{\partial t} + (\boldsymbol{v} \cdot \boldsymbol{\nabla})\boldsymbol{v} = -\boldsymbol{\nabla}\left(\frac{p_1}{\rho_0}\right) + \frac{s_1}{c_p} g\hat{z} + \frac{1}{4\pi\rho_0} (\boldsymbol{\nabla} \times \boldsymbol{B}) \times \boldsymbol{B} + \frac{1}{\rho_0} \boldsymbol{\nabla} \cdot \Pi . \tag{A4}$$

Because we assume periodic boundary conditions for the two horizontal directions (x and y), we spectrally decompose each of the dependent variables:

$$\mathscr{Q} = \sum_m \sum_n \tilde{\mathscr{Q}}_{mn}(z) e^{i2\pi f_m x} e^{i2\pi g_n y} . \tag{A5}$$

Here $\mathscr{Q}$ represents any one of $\mathscr{W}$, $\mathscr{Z}$, $\mathscr{B}$, $\mathscr{J}$, s_1, p_1, etc. In the above $f_m \equiv m/L_x$, $g_n \equiv n/L_y$, where m and n are integers ranging, respectively, from $-N_x/2 + 1$ to $N_x/2$ and from $-N_y/2 + 1$ to $N_y/2$, with N_x and N_y being, respectively, the number of grid points in the x and y directions, and L_x and L_y are the x and y size of the rectangular domain. We generally let N_x and N_y to be powers of 2 to take advantage of the FFT algorithm. In the following, we use F_{mn} to denote $e^{i2\pi f_m x} e^{i2\pi g_n y}$. Using the above spectral decomposition, equations (A1) and (A2) lead to

$$B_z = \sum_m \sum_n 4\pi^2 (f_m^2 + g_n^2) \tilde{\mathscr{B}}_{mn} F_{mn} , \tag{A6}$$

$$B_y = \sum_m \sum_n i2\pi \left(g_n \frac{d\tilde{\mathscr{B}}_{mn}}{dz} - f_m \tilde{\mathscr{J}}_{mn} \right) F_{mn} + \overline{B}_y , \tag{A7}$$

$$B_x = \sum_m \sum_n i2\pi \left(f_m \frac{d\tilde{\mathscr{B}}_{mn}}{dz} + g_n \tilde{\mathscr{J}}_{mn} \right) F_{mn} + \overline{B}_x , \tag{A8}$$

$$(\boldsymbol{\nabla} \times \boldsymbol{B})_z = \sum_m \sum_n 4\pi^2 (f_m^2 + g_n^2) \tilde{\mathscr{J}}_{mn} F_{mn} , \tag{A9}$$

$$\rho_0 v_z = \sum_m \sum_n 4\pi^2 (f_m^2 + g_n^2) \tilde{\mathscr{W}}_{mn} F_{mn} , \tag{A10}$$

$$\rho_0 v_y = \sum_m \sum_n i2\pi \left(g_n \frac{d\tilde{\mathscr{W}}_{mn}}{dz} - f_m \tilde{\mathscr{Z}}_{mn} \right) F_{mn} + \rho_0 \overline{v}_y , \tag{A11}$$

$$\rho_0 v_x = \sum_m \sum_n i2\pi \left(f_m \frac{d\tilde{\mathscr{W}}_{mn}}{dz} + g_n \tilde{\mathscr{Z}}_{mn} \right) F_{mn} + \rho_0 \overline{v}_x , \tag{A12}$$

$$\rho_0 (\boldsymbol{\nabla} \times \boldsymbol{v})_z = \sum_m \sum_n 4\pi^2 (f_m^2 + g_n^2) \tilde{\mathscr{Z}}_{mn} F_{mn} , \tag{A13}$$

where the components $\overline{B}_x(z)$, $\overline{B}_y(z)$, $\overline{v}_x(z)$, $\overline{v}_y(z)$ have been added to represent the horizontal average [i.e., the $(m, n) = (0,0)$ components] of B_x, B_y, v_x, v_y at each height z. We have assumed that $\overline{B}_z(z)$ and $\overline{v}_z(z)$ are zero, i.e., there is no net magnetic flux threading through the upper and lower boundaries, nor there is vertical pulsation in the plane parallel domain. Note that the Fourier components $\tilde{\mathscr{B}}_{00}$, $\tilde{\mathscr{J}}_{00}$, $\tilde{\mathscr{W}}_{00}$, and $\tilde{\mathscr{Z}}_{00}$ do not contribute to determining $\boldsymbol{B}$ and $\boldsymbol{v}$.

From the z-component of equation (5) and the z-component of the curl of equation (5), we obtain the equations for the evolution of $\tilde{\mathscr{B}}_{mn}$ and $\tilde{\mathscr{J}}_{mn}$ (excluding the component with $m = 0$ and $n = 0$):

$$\frac{\partial \tilde{\mathscr{B}}_{mn}}{\partial t} = \frac{1}{4\pi^2 (f_m^2 + g_n^2)} \left[i2\pi f_m \widetilde{(v_z B_x - v_x B_z)}_{mn} - i2\pi g_n \widetilde{(v_y B_z - v_z B_y)}_{mn} \right] - 4\pi^2 (f_m^2 + g_n^2) \eta \tilde{\mathscr{B}}_{mn} + \eta \frac{\partial^2 \tilde{\mathscr{B}}_{mn}}{\partial z^2} , \tag{A14}$$

$$\frac{\partial \tilde{\mathscr{J}}_{mn}}{\partial t} = \frac{1}{4\pi^2 (f_m^2 + g_n^2)} \left[i2\pi g_n \frac{\partial}{\partial z} \widetilde{(v_z B_x - v_x B_z)}_{mn} + i2\pi f_m \frac{\partial}{\partial z} \widetilde{(v_y B_z - v_z B_y)}_{mn} \right]$$

$$+ \widetilde{(v_x B_y - v_y B_x)}_{mn} - 4\pi^2 (f_m^2 + g_n^2) \eta \tilde{\mathscr{J}}_{mn} + \eta \frac{\partial^2 \tilde{\mathscr{J}}_{mn}}{\partial z^2} , \tag{A15}$$

where "$\widehat{(\text{expression})}_{mn}$" represents the Fourier coefficient of the expression under the brace. Similarly, the z-component of the curl of the momentum equation yields the equation for advancing $\tilde{\mathscr{Z}}_{mn}$:

$$\frac{\partial \tilde{\mathscr{Z}}_{mn}}{\partial t} = \frac{1}{4\pi^2(f_m^2+g_n^2)}\left\{-i2\pi g_n\left[\widehat{\left(\frac{\boldsymbol{B}}{4\pi}\cdot\nabla\right)B_x-(\rho_0\boldsymbol{v}\cdot\nabla)v_x}\right]_{mn}+i2\pi f_m\left[\widehat{\left(\frac{\boldsymbol{B}}{4\pi}\cdot\nabla\right)B_y-(\rho_0\boldsymbol{v}\cdot\nabla)v_y}\right]\right\}$$

$$-4\pi^2(f_m^2+g_n^2)\mu\frac{\tilde{\mathscr{Z}}_{mn}}{\rho_0}+\mu\frac{\partial^2}{\partial z^2}\left(\frac{\tilde{\mathscr{Z}}_{mn}}{\rho_0}\right). \tag{A16}$$

The equation for the evolution of $\tilde{\mathscr{W}}_{mn}$ can be derived from the z-component of the momentum equation. This equation contains p_1 on the right-hand side, which is determined by taking the divergence of the momentum equation, and applying the requirement of equation (1). Here however, we use a different approach to solve for the evolution of $\tilde{\mathscr{W}}_{mn}$. We introduce a new quantity $\tilde{\Omega}_{mn}$ defined as

$$\tilde{\Omega}_{mn} = -\frac{1}{4\pi^2(f_m^2+g_n^2)}\left(i2\pi f_m\tilde{\omega}_{ymn}-i2\pi g_n\tilde{\omega}_{xmn}\right), \tag{A17}$$

where $\tilde{\omega}_{xmn}$ and $\tilde{\omega}_{ymn}$ are the Fourier transform coefficients of ω_x and ω_y, which are, respectively, the x- and y-components of the vorticity $\omega \equiv \nabla\times\boldsymbol{v}$. From the x- and y-components of the curl of equation (A4), we obtain equations for the evolution of $\tilde{\omega}_{xmn}$ and $\tilde{\omega}_{ymn}$ and hence determine the evolution of $\tilde{\Omega}_{mn}$:

$$\frac{\partial\tilde{\Omega}_{mn}}{\partial t} = -\frac{i2\pi f_m}{4\pi^2(f_m^2+g_n^2)}\left\{\frac{1}{\rho_0 h_0}\left[\widehat{\left(\frac{\boldsymbol{B}}{4\pi}\cdot\nabla\right)B_x-(\rho_0\boldsymbol{v}\cdot\nabla)v_x}\right]_{mn}+\frac{1}{\rho_0}\frac{\partial}{\partial z}\left[\widehat{\left(\frac{\boldsymbol{B}}{4\pi}\cdot\nabla\right)B_x-(\rho_0\boldsymbol{v}\cdot\nabla)v_x}\right]_{mn}\right\}$$

$$-\frac{i2\pi g_n}{4\pi^2(f_m^2+g_n^2)}\left\{\frac{1}{\rho_0 h_0}\left[\widehat{\left(\frac{\boldsymbol{B}}{4\pi}\cdot\nabla\right)B_y-(\rho_0\boldsymbol{v}\cdot\nabla)v_y}\right]_{mn}+\frac{1}{\rho_0}\frac{\partial}{\partial z}\left[\widehat{\left(\frac{\boldsymbol{B}}{4\pi}\cdot\nabla\right)B_y-(\rho_0\boldsymbol{v}\cdot\nabla)v_y}\right]_{mn}\right\}$$

$$-\frac{1}{\rho_0}\left[\widehat{\left(\frac{\boldsymbol{B}}{4\pi}\cdot\nabla\right)B_z-(\rho_0\boldsymbol{v}\cdot\nabla)v_z}\right]_{mn}-\left[\frac{g}{c_p}\tilde{s}_{1mn}+\frac{1}{8\pi\rho_0 h_0}\widehat{(B^2)}_{mn}\right]$$

$$+\frac{4}{3}\mu 4\pi^2(f_m^2+g_n^2)\frac{\tilde{\mathscr{W}}_{mn}}{\rho_0^2 h_0^2}-4\pi^2(f_m^2+g_n^2)\mu\frac{\tilde{\Omega}_{mn}}{\rho_0}+\mu\frac{\partial}{\partial z}\left(\frac{1}{\rho_0}\frac{\partial\tilde{\Omega}_{mn}}{\partial z}\right). \tag{A18}$$

Further, we can show that $\tilde{\Omega}_{mn}$ and $\tilde{\mathscr{W}}_{mn}$ are related by the equation:

$$\frac{\partial}{\partial z}\left(\frac{1}{\rho_0}\frac{\partial\tilde{\mathscr{W}}_{mn}}{\partial z}\right)-4\pi^2(f_m^2+g_n^2)\frac{1}{\rho_0}\tilde{\mathscr{W}}_{mn}=\tilde{\Omega}_{mn}. \tag{A19}$$

Therefore, once $\tilde{\Omega}_{mn}$ is known, we calculate $\tilde{\mathscr{W}}_{mn}$ by solving the elliptic equation (A19).

In addition, equation (3) gives the equation for the evolution of $\tilde{s}_{1mn}$ (the Fourier coefficients of s_1):

$$\frac{\partial\tilde{s}_{1mn}}{\partial t} = -4\pi^2(f_m^2+g_n^2)\frac{\tilde{\mathscr{W}}_{mn}}{\rho_0}\frac{ds_0}{dz}-i2\pi f_m\widehat{(v_x s_1)}_{mn}-i2\pi g_n\widehat{(v_y s_1)}_{mn}-\frac{1}{\rho_0}\frac{\partial}{\partial z}\widehat{(\rho_0 v_z s_1)}_{mn}$$

$$-4\pi^2(f_m^2+g_n^2)K\tilde{s}_{1mn}+K\frac{1}{T_0}\frac{\partial}{\partial z}\left(T_0\frac{\partial\tilde{s}_{1mn}}{\partial z}\right)$$

$$+\frac{1}{\rho_0 T_0}\left\{\frac{\eta}{4\pi}\left(\widehat{|\nabla\times\boldsymbol{B}|^2}\right)_{mn}+\widehat{[(\Pi\cdot\nabla)\cdot\boldsymbol{v}]}_{mn}\right\}. \tag{A20}$$

Therefore, in summary, we have equations (A14), (A15), (A16), (A18), (A19), and (A20) to determine the evolution of the dependent variables $\tilde{\mathscr{B}}_{mn}(z)$, $\tilde{\mathscr{J}}_{mn}(z)$, $\tilde{\mathscr{Z}}_{mn}(z)$, $\tilde{\Omega}_{mn}(z)$, $\tilde{\mathscr{W}}_{mn}(z)$, and $\tilde{s}_{1mn}(z)$. Note that equations (A14)–(A19) are only defined for the Fourier components with $(m, n) \neq (0,0)$. The components $\tilde{\mathscr{B}}_{00}(z)$, $\tilde{\mathscr{J}}_{00}(z)$, $\tilde{\mathscr{Z}}_{00}(z)$, $\tilde{\Omega}_{00}(z)$, and $\tilde{\mathscr{W}}_{00}(z)$ are not used because they do not affect $\boldsymbol{B}$ and $\boldsymbol{v}$. However, we do need a separate set of equations for determining the evolution of $\overline{B}_x(z)$, $\overline{B}_y(z)$, $\overline{v}_x(z)$, and $\overline{v}_y(z)$. These equations can be derived by taking horizontal averages of the induction equation (5) and the momentum equation (2):

$$\frac{\partial\overline{B}_x}{\partial t} = \frac{\partial}{\partial z}\left(\overline{v_x B_z}-\overline{v_z B_x}\right)+\eta\frac{\partial^2\overline{B}_x}{\partial z^2}, \tag{A21}$$

$$\frac{\partial \overline{B}_y}{\partial t} = \frac{\partial}{\partial z}\left(\overline{v_y B_z} - \overline{v_z B_y}\right) + \eta \frac{\partial^2 \overline{B}_y}{\partial z^2}, \tag{A22}$$

$$\frac{\partial}{\partial t}\left(\rho_0 \overline{v}_x\right) = \frac{\partial}{\partial z}\left(\frac{1}{4\pi}\overline{B_z B_x} - \rho_0 \overline{v_z v_x}\right) + \mu \frac{\partial^2 \overline{v}_x}{\partial z^2}, \tag{A23}$$

$$\frac{\partial}{\partial t}\left(\rho_0 \overline{v}_y\right) = \frac{\partial}{\partial z}\left(\frac{1}{4\pi}\overline{B_z B_y} - \rho_0 \overline{v_z v_y}\right) + \mu \frac{\partial^2 \overline{v}_y}{\partial z^2}. \tag{A24}$$

All the equations for the Fourier variables [$\tilde{\mathscr{B}}_{mn}(z)$, $\tilde{\mathscr{J}}_{mn}(z)$, $\tilde{\mathscr{E}}_{mn}(z)$, $\tilde{\Omega}_{mn}(z)$, $\tilde{\mathscr{W}}_{mn}(z)$, $\tilde{s}_{1mn}(z)$, and $\overline{B}_x(z)$, $\overline{B}_y(z)$, $\overline{v}_x(z)$,$\overline{v}_y(z)$] are then discretized with respect to the vertical (z) direction, with the vertical derivatives being approximated by their fourth-order centered differences:

$$\left(\frac{dq}{dz}\right)_k = \frac{4}{3}\frac{q(z_{k+1}) - q(z_{k-1})}{2\Delta z} - \frac{1}{3}\frac{q(z_{k+2}) - q(z_{k-2})}{4\Delta z}, \tag{A25}$$

$$\left(\frac{d^2q}{dz^2}\right)_k = \frac{4}{3}\frac{q(z_{k+1}) - 2q(z_k) + q(z_{k-1})}{\Delta z^2} - \frac{1}{3}\frac{q(z_{k+2}) - 2q(z_k) + q(z_{k-2})}{4\Delta z^2}, \tag{A26}$$

where $q(z)$ denotes any function of z and Δz is the grid spacing in the vertical direction.

The discretized equations for the Fourier variables are time advanced using a semi-implicit method. Using operator splitting (Press et al. 1992, p. 847), we apply the second-order Adams-Bashforth scheme for the advection terms and the second-order Crank-Nicolson scheme for the diffusion terms. To illustrate this, we use equation (A14) as an example, which we rewrite into the following schematic form:

$$\frac{\partial \tilde{\mathscr{B}}_{mn}}{\partial t} = \mathscr{O}_1(\tilde{\mathscr{Q}}_{mn}) + \mathscr{O}_2(\tilde{\mathscr{B}}_{mn}), \tag{A27}$$

where $\mathscr{O}_1$ represents the first term on the right-hand side of equation (A14), $\tilde{\mathscr{Q}}_{mn}$ denotes all of the dependent variables involved in that term, and $\mathscr{O}_2$ represents the remainder two diffusion terms. We advance $\tilde{\mathscr{B}}_{mn}$ from time step j: $\tilde{\mathscr{B}}^j_{mn}$, to time step $j+1$: $\tilde{\mathscr{B}}^{j+1}_{mn}$, by the following sequence of updating:

$$\tilde{\mathscr{B}}^{j+1*}_{mn} = \tilde{\mathscr{B}}^j_{mn} + \Delta t[\tfrac{3}{2}\,\mathscr{O}_1(\tilde{\mathscr{Q}}^j_{mn}) - \tfrac{1}{2}\,\mathscr{O}_1(\tilde{\mathscr{Q}}^{j-1}_{mn})], \tag{A28}$$

$$\tilde{\mathscr{B}}^{j+1}_{mn} = \tilde{\mathscr{B}}^{j+1*}_{mn} + \Delta t\,\tfrac{1}{2}\,[\mathscr{O}_2(\tilde{\mathscr{B}}^{j+1*}_{mn}) + \mathscr{O}_2(\tilde{\mathscr{B}}^{j+1}_{mn})], \tag{A29}$$

where the first step updates $\tilde{\mathscr{B}}_{mn}$ for the operator $\mathscr{O}_1$ with the Adams-Bashforth scheme, yielding an intermediate result $\tilde{\mathscr{B}}^{j+1*}_{mn}$, and then the second step updates $\tilde{\mathscr{B}}_{mn}$ for the diffusion terms using the Crank-Nicolson scheme. The latter step requires solving a penta-diagonal system of linear equations.

REFERENCES

Batchelor, G. K. 1967, An Introduction to Fluid Dynamics (Cambridge: Cambridge Univ. Press)
Emonet, T., & Moreno-Insertis, F. 1998, ApJ, 492, 804
Fan, Y., Zweibel, E. G., & Lantz, S. R. 1998a, ApJ, 493, 480
Fan, Y., Zweibel, E. G., Linton, M. G., & Fisher, G. H. 1998b, ApJ, 505, L59
Freidberg, J. P. 1982, Rev. Mod. Phys., 54, 801
Gilman, P. A., & Glatzmaier, G. A. 1981, ApJS, 45, 335
Glatzmaier, G. A. 1984, J. Comp. Phys., 55, 461
Lamb, H. 1945, Hydrodynamics (New York: Dover)
Lantz, S. R., & Fan, Y. 1999, ApJS, 121, 247
Leka, K. D., Canfield, R. C., McClymont, A. N., & van Driel-Gesztelyi, L. 1996, ApJ, 462, 547
Leka, K. D., van Driel-Gesztelyi, L., Nitta, N., Canfield, R. C., Mickey, D. L., Sakurai, T., & Ichimoto, K. 1994, Sol. Phys., 155, 301
Linton, M. G., Dahlburg, R. B., Fisher, G. H., & Longcope, D. W. 1998, ApJ, 507, 404
Linton, M. G., Fisher, G. H., Dahlburg, R. B., & Fan, Y. 1999, ApJ, submitted
Linton, M. G., Longcope, D. W., & Fisher, G. H. 1996, ApJ, 469, 954
Lites, B. W., & Low, B. C. 1997, Sol. Phys., 174, 91
Lites, B. W., Low, B. C., Martinez Pillet, V., Seagraves, P., Skumanich, A., Frank, Z. A., Shine, R. A., & Tsuneta, S. 1995, ApJ, 446, 877
Longcope, D. W., Fisher, G. H., & Arendt, S. 1996, ApJ, 464, 999
Longcope, D. W., Fisher, G. H., & Pevtsov, A. A. 1998, ApJ, 507, 417
Low, B. C. 1996, Sol. Phys., 167, 217
Matsumoto, R., Tajima, T., Chou, W., Okubo, A., & Shibata, K. 1998, ApJ, 493, L43
McClymont, A. N., & Fisher, G. H. 1989, in Solar System Plasma Physics, ed. J. H. Waite, J. L. Burch, & R. L. Moore (Washington: American Geophys. Union), 219
Moreno-Insertis, F., & Emonet, T. 1996, ApJ, 472, L53
Parker, E. N. 1975, ApJ, 198, 205
———. 1979, Cosmical Magnetic Fields (Oxford: Oxford University Press)
Press, W. H., Teukolsky, S. A., Vetterling, W. T., & Flannery, B. P. 1992, Numerical Recipes in FORTRAN (Cambridge: Cambridge Univ. Press)
Schüssler, M. 1979, A&A, 71, 79
Spruit, H. C., & van Ballegooijen, A. A. 1983, A&A, 106, 58
Tanaka, K. 1991, Sol. Phys., 136, 133
Zirin, H. 1998, Astrophysics of the Sun (Cambridge: Cambridge Univ. Press)